Effect of oxygen content on elastic properties of an oxygen-graded titanium: Experimental and computational analyses

Ayyoub Dziri, Kais Ammar, Samuel Forest, Henry Proudhon, Quentin Sirvin, Thiebaud Richeton, Damien Texier

Materials & Design 259 (2025) 114801

Contents lists available at ScienceDirect

Materials & Design

journal homepage: www.elsevier.com/locate/matdes

Effect of oxygen content on elastic properties of an oxygen-graded titanium: Experimental and computational analyses

Ayyoub Dziri[a,b], Kais Ammar[b], Samuel Forest[b], Henry Proudhon[b], Quentin Sirvin[a], Thiebaud Richeton[c], Damien Texier[a,*]

[a] Institut Clement Ader (ICA) - UMR CNRS 5312, Université de Toulouse, CNRS, INSA, UPS, Mines Albi, ISAE-SUPAERO, Campus Jarlard, 81013 Albi Cedex 09, Toulouse, France
[b] Mines Paris, PSL University, MAT - Centre des matériaux, CNRS UMR 7633, BP 87, 91003 Evry, France
[c] Université de Lorraine, CNRS, Arts et Métiers Institute of Technology, LEM3, F-57000 Metz, France

HIGHLIGHTS

- Improved correlative mechanical microscopy in O-graded Ti using wedge-cut sample compared to conventional cross-section samples.
- Better identification of the spatial dependence of the Young's modulus in Ti-O system.
- The anisotropic elastic response of aggregates with different sets of crystallographic orientations and ORL extensions was evaluated using finite element simulations.
- Short oxidation exposure is detrimental for the mechanical integrity of oxidized Ti-alloys due to greater average stresses but also maximal values.
- Adherent TiO_2 oxide induced greater but more homogeneous stress concentration at the metal/oxide interface under a given pre-oxidation condition.

GRAPHICAL ABSTRACT

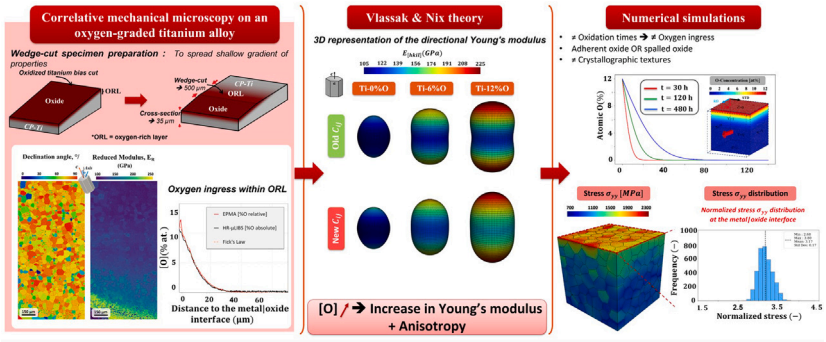

ARTICLE INFO

Keywords:
Commercially pure titanium
Oxidation
Oxygen ingress
Nanoindentation
Elastic anisotropy
Polycrystalline mechanical modeling

ABSTRACT

High-speed nanoindentation mapping (HSNM), electron backscatter diffraction (EBSD), electron microprobe analyses (EPMA), and high resolution – microscale laser induced breakdown spectroscopy (HR–µLIBS), were used to characterize the evolution of the elastic anisotropy of a commercially pure titanium (CP-Ti) having a gradient of oxygen concentration. CP-Ti samples were pre-oxidized in air at 655 °C for 120 h to create a 35 μm-deep gradient of oxygen within Ti, the oxygen-rich layer (ORL). Wedge-cut samples were prepared to spread the ORL over hundreds of micrometers instead of tens of micrometers for cross-sections. EPMA and HR–µLIBS were used to quantify the oxygen distribution within the ORL in a relative and absolute manner, respectively. The Vlassak-Nix theory was used for inverse identification of the stiffness matrix terms as a function of the oxygen content. The stiffness matrix as a function of the oxygen concentration was used to simulate the stress–strain distribution at

* Corresponding author.
Email address: damien.texier@mines-albi.fr (D. Texier).

https://doi.org/10.1016/j.matdes.2025.114801
Received 18 June 2025; Received in revised form 19 August 2025; Accepted 18 September 2025
Available online 22 September 2025

the sub-grain level in the ORL under tensile macroscopic loading. Configurations with and without external oxide were numerically tested to investigate the role of the oxide layer on the stress distribution within the ORL as well as the crystallographic texture.

1. Introduction

Titanium and its alloys are highly valued metallic materials in industry due to their superior specific properties such as low density, high mechanical strength, good corrosion resistance and their ability to maintain their properties at high temperatures. For these reasons, they are widely used for manufacturing aircraft structures, engines and critical components [1,2]. They are also used in the biomedical industry, especially for bone implants and medical devices due to their biocompatibility and corrosion resistance [3,4]. In the energy field, titanium is used in nuclear reactors, geothermal pipes and secondary circuits of heat exchangers due to its corrosion and erosion resistance [5]. However, titanium and its alloys have a significant drawback: their ability to capture and dissolve oxygen, making them particularly sensitive to oxygen embrittlement. Upon contact with oxygen in air or water, a passive oxide layer, mainly titanium dioxide (TiO_2), forms immediately on the surface. In high-temperature applications, oxygen can also dissolve in the titanium metal and form a hard and brittle oxygen-rich zone beneath the external oxide layer, the so-called oxygen-rich layer (ORL) [6]. Oxygen dissolution depends on the allotropic version of titanium, *i.e.*, the α-hexagonal close-packed (HCP) - titanium (Ti) or β-face centered cubic (FCC) - titanium (Ti) [7,8]. For given temperature and exposure conditions, the ORL can lead to the formation of an α-rich layer at the extreme surface, the so-called α-case layer. The brittle character of the ORL is yet important regardless of the presence or not of the α-case layer. Therefore, investigation of oxygen ingress and its impact on the mechanical integrity of titanium alloys is of prime interest for high-temperature applications where oxygen ingress is a concern.

Titanium oxidation changes mainly as a function of the temperature and the environment in which it evolves. At high temperature, *i.e.*, temperatures approaching 500 °C – 600 °C, the oxidation rate of titanium follows a parabolic law due to the formation of a compact oxide layer of TiO_2 and oxygen ingress in the early stage of oxidation. After a brief period, the oxidation behavior deviates from the parabolic regime and is generally followed by a higher oxidation rate (pseudo-linear kinetics), as a result of the loss of the oxide protective barrier. The oxide layer repeatedly spalls off as it approaches a critical thickness due to growth stresses and/or thermal stresses caused by cyclic oxidation. At temperatures between 650 °C and 700 °C, the oxide layer becomes thicker and oxygen diffusion into titanium is more significant [9]. As far as the oxygen dissolution is concerned, it is typically assumed that the solubility limit of oxygen into titanium can reach up to 33 at% solubility in α-Ti for temperatures close to 650 °C [8,10]. However, in the case of high-temperature oxidation, the oxygen concentration at the metal/oxide interface is variable in literature [11–13]. This interfacial concentration, ranging from 12 to 25 at% depending on the exposure temperature and duration, does not reach the maximal solubility limit of O within Ti. It is also worth reminding that the solubility limit of oxygen within the β-Ti phase is much lower (8 at%) than within the α and can lead to heterogeneous oxygen distribution in the two-phase titanium alloys. Diffusion of oxygen atoms into α-titanium occurs preferentially through the octahedral sites of the hexagonal lattice, allowing oxygen insertion. Energy barriers to enable oxygen mobility inside the α-Ti lattice are grain-orientation dependent but also chemically dependent due to attractive/repulsive interactions between atoms [14,15]. Nitrogen and the formation of particular nitrides can also modify the progressive ingress of O within Ti [16–20]. All these aspects can make oxygen distribution particularly heterogeneous at the microstructure scale. However, Magazzeni et al. [21] reported a homogeneous distribution of O within Ti at the microstructure scale for a grade 2 commercially pure titanium (CP-Ti) after high temperature oxidation using microprobe analyses (EPMA). Furthermore, the anisotropic and heterogeneous oxygen diffusion of O within Ti is generally neglected in the literature and 1-dimensional diffusion profiles are used to quantify oxygen diffusion within Ti [22].

Oxygen insertion in titanium has a significant impact on the mechanical properties of titanium. Its insertion in octahedral sites leads to an increase in lattice volume with a greater increase in the *c*-axis direction relative to the *a*-axis one (by a factor of 2) [23,24]. This anisotropic lattice expansion also impairs the dislocation mobility and binding energy, thus modifying the deformation behavior [25–27]. The evolution of the mechanical properties of titanium as a function of the oxygen content has been widely investigated at low oxygen concentrations using bulk materials with homogeneous oxygen contents [27–30]. More recently, micromechanical approaches aimed at characterizing the effect of greater oxygen contents on the mechanical properties of titanium at the ORL scale. This zone, particularly rich in oxygen at the metal/oxide interface, presents a gradient of oxygen concentration and can extend up to ten times the thickness of the oxide layer. The ORL plays a crucial role in the mechanical behavior and integrity of oxidized titanium components, especially under cyclic conditions [31–33]. Understanding and predicting the mechanical behavior of the ORL as a function of the local oxygen content is a central question to consider the mechanical integrity and sensitivity to oxygen embrittlement as a function of temperature, time, and applied stress. To investigate this phenomenon, Sirvin et al. [34,35] used an innovative approach: microtensile tests on pre-oxidized ultrathin samples of varying thicknesses, where the samples were subjected to pre-oxidation treatments at 700 °C for different durations, thus creating specimens with various ratios between ORL and the non-affected material (NAM). This approach enabled to demonstrate the competition between strengthening effects due to oxygen enrichment and the development of early damage/cracking in the peripheral material. Strain-to-fracture considerably decreased with increasing oxidation time, illustrating the embrittling effect of oxygen. Furthermore, Oh et al. [36] reported that the elongation of the CP-Ti considerably decreased as the oxygen concentration increased, where the measured elongation values of the CP-Ti ingots were 18.2 %, 13.1 %, 10.3 % and 7.2 % for oxygen concentrations varying from 1310 ppm, 1880 ppm, 2830 ppm to 3510 ppm, respectively. Indeed, while most results in the literature follow a linear trend, showing a progressive and significant decrease in strain-to-failure with the addition of oxygen, Amann et al. [30] observed an appreciable ductility (around 30 %) up to 0.6 wt %, then a sharp drop beyond this value. They attributed the high elongation to the presence of Ti_6O precipitates, which in turn may play a major role in maintaining elongation-to-fracture despite high concentrations of oxygen, as also confirmed by Sun et al. [37] and Wasz et al. [38]. However, oxygen concentration within the ORL can reach much greater oxygen concentration in the vicinity of the metal/oxide interface and the fabrication and mechanical testing of bulk titanium materials with homogeneous and high concentrations of oxygen is a challenge. Therefore, micromechanical approaches, including nanoindentation, aimed to assess local mechanical within the ORL, the extension of the ORL being sometimes a challenge for further statistical testing based on the tens-of-micrometer affected depth. While microhardness and nanoindentation are adopted techniques for decades to document the strengthening effect of oxygen within the ORL, only one-dimensional profiles, similar to EPMA results reported in the literature, are generally proposed [28,29,31–33,39–44]. However, developments in single indentation and nanoindentation mapping aimed at dissociating the hardness response as a function of the crystal orientation for CP-Ti materials [21,45–53]. Indeed, grains with the *c*-axis direction perpendicular to the nanoindentation direction exhibit a nearly

40 %–70 % softer hardness than grains with the *c*-axis direction parallel to the nanoindentation direction. Similar trends were also observed for the evolution of directional elastic properties, despite more complicated to obtain based on the low elastic anisotropy of CP-Ti materials. Highly resolved nanoindentation mapping aimed at documenting the evolution of the hardness response as a function of the grain orientation and oxygen uptake within the ORL [21,53]. As far as the evolution of the anisotropic elastic response as a function of the oxygen content is concerned, a recent work used inverse identification methods based on the Vlassak and Nix model [54,55] to assess the evolution of the stiffness matrix as a function of the oxygen concentration [53]. In this paper, nanoindentation was performed on a pre-oxidized specimen on cross-section plane, the ORL extending over 45 μm in depth. Based on the spatial resolution of high speed nanoindentation mapping (HSNM) and potential size effects, the step size between measurements limited the evaluation of mechanical properties for a given oxygen content in the oxygen-very rich layer due to sharp oxygen variations over micrometers near the metal/oxide interface. However, the authors evidenced a severe increase in elastic anisotropy with the oxygen content, with a particular increase of the stiffness along the *c*-axis direction of the hexagonal crystal due to oxygen insertion in octahedral sites (1.4 at 0.05 at% compared to 2.1 at 20.0 at%). Therefore, the present paper intends to enhance the HSNM response of pre-oxidized CP-Ti specimens using wedge-cut preparation to spread the tens-of-micrometers deep ORL over hundreds-of-micrometers region of interest to increase both spatial resolution and statistical analyses. Knowledge of the elastic anisotropy and global property evolution is highly important in property-graded materials to better understand and evaluate internal stress–strain distribution due to the heterogeneous mechanical response of polycrystalline aggregates.

In this paper, a method for characterizing pre-oxidized titanium using wedge-cut polishing has been developed, combining crystallographic information from electron backscattered diffraction (EBSD), chemical data from electron beam microanalysis (EPMA) and high resolution – microscale laser induced breakdown spectroscopy (HR–μLIBS), and mechanical property data from high speed nanoindentation mapping (HSNM). The wedge-cut polishing technique was purposely used to spread the tens-of-micrometer deep gradient of oxygen over hundreds of micrometers to allow for a more precise characterization of the oxygen-rich layer (ORL) using HSNM, EBSD, EPMA and HR–μLIBS. The evolution of the elastic properties at the sub-grain level was thus investigated as a function of the local crystallographic orientation and the oxygen concentration. The identification of the stiffness matrix as a function of the oxygen concentration was revised from Ref. [53] based on the more appropriate spatial resolution of the wedge-cut preparation. The revised stiffness matrix was used to simulate the stress–strain distribution at the sub-grain level within the ORL under tensile macroscopic load, to study the local stress distribution from surface to metal core as a function of oxygen ingress within the framework of linear elasticity. The effects of both the ORL extension and grain size on the elastic response of polycrystalline aggregates were investigated using the finite element method.

2. Material and experimental methods

2.1. Material and sample preparation

The material used in this study was a 1.8 mm-thick rolled plate of grade 2 CP-Ti with a nominal composition of Ti-0.14% O-0.07% Fe 0.0% N-0.0% C (wt %) provided by Nippon Steel and Sumitomo Metal Corp. Samples with dimensions of $19 \times 5 \times 1.8$ mm^3 were extracted from the plate. The geometry of the sample and direction related to the rolling process are depicted in Fig. 1(a): the rolling direction (RD), the long transverse direction (LTD), and the short transverse direction (STD) corresponding to the specimen thickness direction (also called ND for normal direction in the literature). The initial material has an α-phase equiaxed-grain microstructure and an average grain size of 20 ± 5 μm. Samples were then vacuum annealed at 855 °C for 24 hours for grain growth and producing an equiaxed-grain microstructure with a larger grain size of 90 ± 5 μm. The microstructure of the as-received and heat-treated samples are presented in Fig. 1(b) and (c), respectively, using grain orientation modality (EBSD maps using inverse pole figure in reference to the LTD direction). This direction was chosen for further oxidation and nanoindentation purposes based on the lower texture level compared to the other rolling process directions, as reported in a preliminary work [53].

The heat-treated sample was then cross-sectioned to oxidize the RD-STD face, to further probe the sample along the LTD direction with nanoindentation. A particular care was taken during cross-section preparation. The sample was bonded on both sides by sacrificial samples to avoid edge effects during polishing (Step 1). The sample was then polished using SiC papers ranging from P600 to P4000. Both sacrificial materials were removed before cleaning. Using an ultrasonic bath, the sample was cleaned for 15 min in acetone, then in ethanol, before high temperature oxidation in air at 655 °C for 120 h, with the face of interest, *i.e.*, the RD-STD face facing the air (Step 2).

After oxidation, the sample was prepared using wedge-cut method to spread the tens-of-micrometer gradient of oxygen in depth over hundreds of micrometers. This method consisted of imposing a controlled tilt of 1.5° using a 500 μm spacer during precision cutting. Again, the oxidized sample was bonded between two sacrificial materials (using cyanoacrylate glue) before cutting to further limit edge effects during polishing in Fig. 2). The back of the sample was then cut using a precision-cutting machine. The sample was glued onto a rectified glass support with sacrificial materials for stability during precision polishing [56] (Step 3). The polishing step with the precision Jig aimed to ensure a good control of the sample parallelism, with SiC paper starting from P1200 to P4000, finishing with colloidal silica of 0.05 μm to obtain a mirror surface (Step 4). The final surface obtained is in the form of an inclined part containing the oxide and a flat face (area of interest) containing at the same time the oxide, the oxygen-enriched zone and the metal core (CP-Ti material in gray in the Step 4 in Fig. 2).

2.2. Distance from the metal/oxide interface using laser scanning confocal microscopy (LSCM)

Laser scanning confocal microscopy was used to assess the topography of the wedge-cut sample to evaluate the distance from the metal/oxide interface on the polished surface. A LEXT Olympus OLS5100 (now EVIDENT) equipped with a 405 nm wavelength laser was used. Topographic measurements were performed using an MPLAPON20XLEXT lens in stitching mode to achieve a good compromise in terms of spatial resolution and height variation sensitivity. Gwyddion software was then used for raw data reading and post-treatment for the surface flatness correction [57]. The external surface with the oxide scale was considered flat and at 0 altitude to further consider each height as the distance from the metal/oxide interface (the height offset was also corrected from surface and optical observations).

2.3. Electron backscatter diffraction (EBSD)

The sample was then analyzed using a JEOL JSM 7100F scanning electron microscope (SEM) equipped with a Symmetry S2 electron backscatter diffraction (EBSD) CMOS detector (Oxford Instruments) to assess the local crystallographic orientation of each grain present on the wedge-cut. Further post-processing of EBSD data was done using the MTex [58] and the open-source Pymicro library[1] for further correlative mechanical microscopy. The declination angle, °/, was considered for further analyses and represents the angle between the normal direction to the surface and the *c*-axis of the α-Ti lattice.

[1] https://github.com/heprom/pymicro. [59]

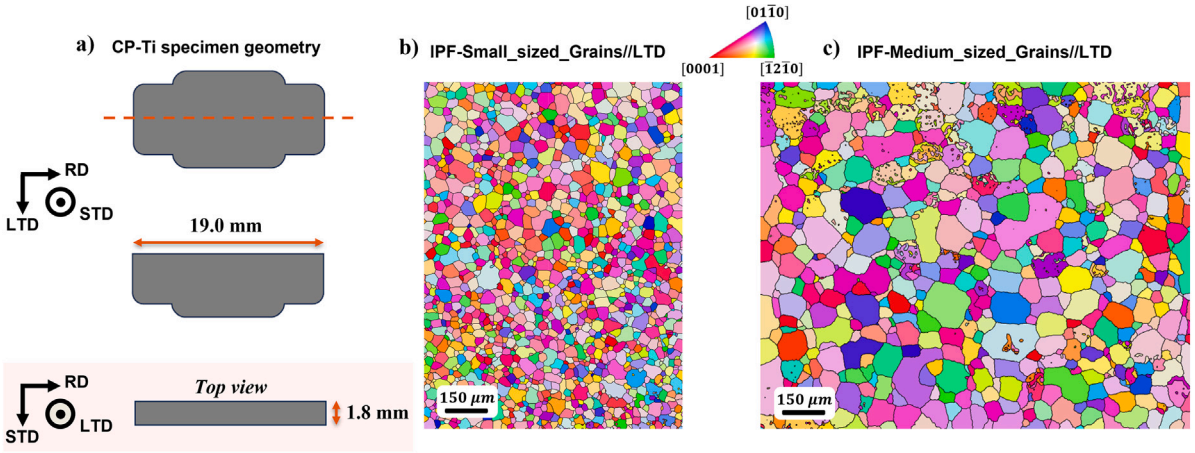

Fig. 1. Commercially pure titanium (CP-Ti) material: (a) sample geometry (dimensions are in mm), (c) EBSD map of the as-received sample with the IPF in reference to LTD (grain size ≃ 20 ± 5 μm), (c) EBSD map of the heat-treated sample with the IPF in reference to LTD (grain size ≃ 90 ± 5 μm).

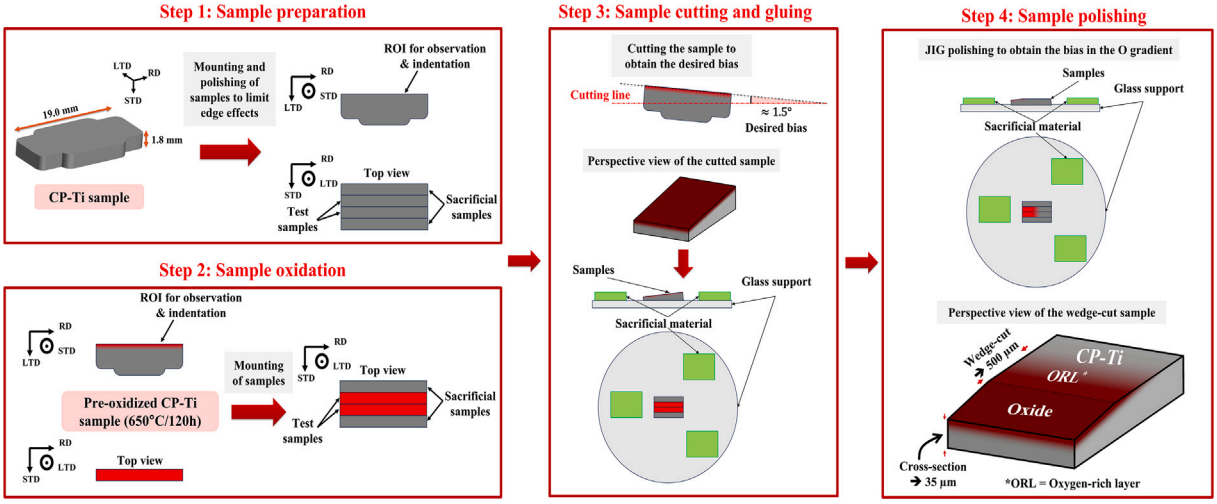

Fig. 2. Wedge-cut preparation procedure of the pre-oxidized CP-Ti sample.

2.4. Oxygen profile using microprobe analysis (EPMA)

Electron Probe Micro-Analyzer (EPMA) was used to determine the local chemical composition of the pre-oxidized CP-Ti material on the wedge-cut surface. Analyses were performed on a CAMECA SX FIVE FE microprobe (FEG source) at an accelerating voltage of 10 kV and 40 nA for the beam current with a dwell time of 2 seconds per spot. A regular square-grid with a pitch of 6 μm was performed. Different standards were used for quantitative measurements: Fe_2O_3 for O-K_α and Fe-K_α, TiO for Ti-K_α and wollastonite for Si-K_α. A particular attention was paid to the specimen preparation to limit edge blunting and the formation of the native TiO_2 [60]. After polishing and cleaning (acetone then ethanol ultrasound cleaning), the sample was coated with a thin carbon layer then stored in a vacuum chamber (10^{-5} mbar) before EPMA analyses. Due to passivation of titanium at room temperature, the oxygen content was measured relative to a reference state, *i.e.*, the non-oxidation affected material. Spectrum subtraction of the oxygen intensity (5 measurements in the bulk) was applied to the whole oxygen profile for correction. Therefore, the oxygen content presented using EPMA in the paper does not correspond to the absolute oxygen content, but the oxygen uptake due to oxygen dissolution during oxidation, and is denoted Δ[O]. 200 oxygen concentration profiles were acquired on the wedge-cut sample to assess the oxygen distribution using EPMA analysis.

2.5. Oxygen profile using high resolution-laser induced breakdown spectroscopy at the microscale (HR–μLIBS)

Oxygen characterization profiles using high resolution-laser induced breakdown spectroscopy at the microscale (HR–μLIBS) were performed using the L-HMA Pro by Lasalys measuring instrument. After the EPMA analysis, the surface of the wedge-cut sample was smoothly refreshed using colloidal silica 0.05 μm polishing then cleaning using abundant water, then ethanol cleaning in ultrasound bath. The energy source was a 20 Hz pulsed laser, with each shot corresponding to a measurement, providing concentration information at the microscale. Oxygen characterization was carried out at a laser energy of 7.5 μJ, with a step size of 3 μm and a wavelength of 777.3 nm. Each crater had approximately a diameter and depth of 2.5 μm. The wedge-cut sample was mounted in cold-low shrinkage epoxy after nanoindentation and slightly polished to remove the nanoindentation imprints (200–300 nm material based on larger imprints for positioning). The sample surface was prepared for a mirror-polished surface finish. The measurement rate was of 20 measurements per second, including stage displacement operations. External standards with homogeneous but different and known oxygen contents were used to calibrate the intensity as a function of the oxygen content. Low-oxygen certified standards used in the present calibration have an oxygen concentration of 450, 1300, 1790, 2460 and 3650 ppm wt. (*i.e.*, 0.13, 0.39, 0.53, 0.73 and 1.08 at. % of O, provided by TECHLAB,

Table 1
Nanoindentation parameters in CSM mode and displacement control mode.

Parameters	O-graded Ti (treated at 855 °C)
Array size (μm^2)	1300 × 2680
Step size (μm)	5 × 5, 5 × 4, 5 × 3, 5 × 2.5, 5 × 2
Array size (indent^2)	260 × 300, 260 × 150, 260 × 150, 260 × 280
Max depth (nm)	100
Load rate (nm·s^{-1})	50
CSM frequency (Hz)	70
Displacement amplitude (nm)	3
Stiffness (kN·mm^{-1})	20,000

France). Titanium samples richer in oxygen were sintered at CIRIMAT Laboratory by Gautier et al. [61] and have an oxygen concentration of 1,9000 , 46,000 and 139,000 ppm wt. (*i.e.*, 5.48, 12.61, and 32.57 at. % of O). Each standard was measured using a 50 × 50 measurement grid, *i.e.*, 2500 shots with the same parameters than the profiles.

2.6. Mechanical characterization

In this work, high speed nanoindentation mapping (HSNM) was performed with a customed FT-I04 nanoindentation system from Femtotools^{AG}, equipped with a diamond Berkovich tip (the calibration of the diamond Berkovich tip was done on fused silica using the continuous stiffness measurement (CSM) technique in displacement-controlled mode and stable values of E_R and H for the fused silica ranged from 20 to 160 nm [53]) and a 20 mN load cell with a position noise floor ± 0.05 nm and a load noise of ± 0.05 μN (MEMS sensor). Nanoindentation tests were performed in CSM mode, with a constant displacement rate. This mode allows the stiffness S to be continuously recorded during the penetration of the indenter. The hardness H and the reduced modulus E_R were thus determined as a function of the penetration depth. The nanoindentation tests were performed at room temperature. The pitch between the different indentations was adapted based on the local oxygen content, the slope of the oxygen profile being steeper close to the metal/oxide interface. Therefore, the pitch between the indentations was refined close to the metal/oxide interface (5 × 2 μm, 2 μm being along the oxygen ingress direction) and progressively larger in the material bulk (5 × 5 μm). This reduction in the distance of steps was for the purpose of extracting more data on mechanical local properties as a function of the local oxygen content for correlative mechanical microscopy. The nanoindentation maps were then interpolated at 1 μm in each direction using linear interpolation for visualization purposes and data merging for alignment. Raw data were used for correlative mechanical microscopy. The nanoindentation parameters for each nanoindentation map are reported in Table 1.

3. Experimental results

3.1. Measurement of the distance to the metal/oxide interface on the wedge-cut sample

Topographic measurements were first performed on the wedge-cut sample using LSCM to accurately establish a relationship between the in-plane spatial position of the wedge-cut surface and the distance to the metal/oxide interface in depth. The optical image of the wedge-cut sample is shown in Fig. 3(a), the white dashed rectangle corresponding to the further region of interest for the correlative mechanical microscopy analysis. The rotation-corrected height map is depicted in Fig. 3(b). The corrected height profile is also illustrated to visualize the applied rotation (Fig. 3(c)). A sixth degree polynomial law was fitted in the region of interest to quantitatively determine the distance to the metal/oxide interface as a function of the distance on the wedge-cut surface for chemical profile analyses. The rotation-corrected height map was used for further inverse identification of the elastic stiffness matrix using correlative mechanical microscopy.

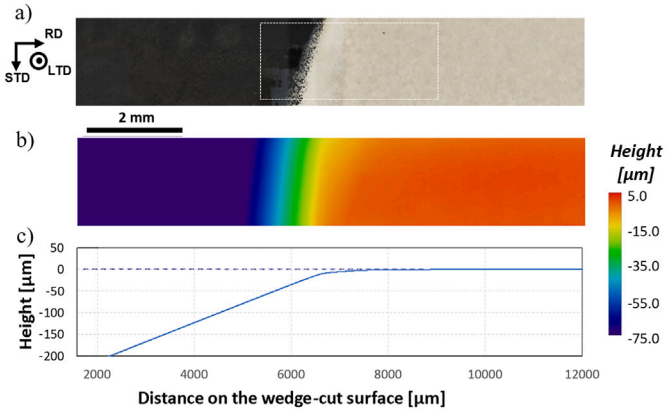

Fig. 3. Optical observation and height map obtained using the LSCM: (a) Optical micrograph of the sample. The further region of interest (ROI) is marked with a white rectangular dashed contour, (b) Rotation-corrected height map, (c) Rotation-corrected height profile along the sample.

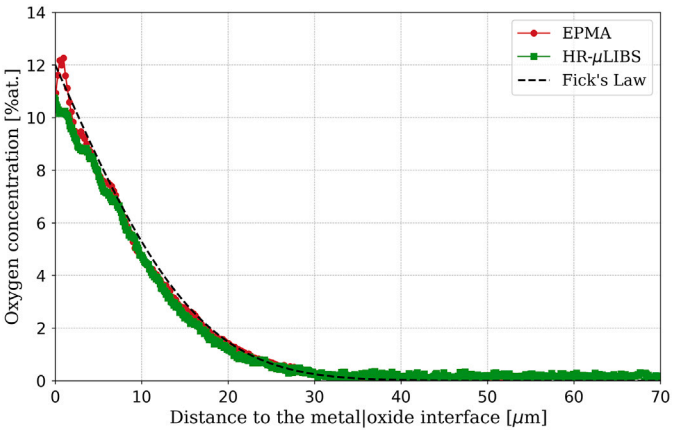

Fig. 4. Oxygen profile in a CP-Ti material after 655 °C – 120 h exposure assessed by EPMA and HR-μLIBS and associated erf function fitting of the second Fick's law.

3.2. Measurement of the oxygen profile

Both EPMA and HR-μLIBS techniques were used to assess the oxygen distribution within the ORL on the wedge-cut surface. Oxygen profiles were registered with the rotation-corrected height map to establish a relationship between the oxygen content and the distance to the metal/oxide interface (see Fig. 4). It is worth mentioning that EPMA measurements are probing the oxygen content relative to the bulk concentration while the HR-μLIBS measurements provide absolute oxygen contents. 200 profiles were averaged for each measurement technique to describe the oxygen profile within the ORL. Diffusion profile results assessed by EPMA and HR-μLIBS are in very good agreement, validating both the techniques. The motivation was to identify both the oxygen concentration at the metal/oxide interface $[O]_s$ and the coefficient of diffusion of O within Ti D_O^{Ti}.

Since the sample was thick enough (few millimeters) compared to the extension of the ORL (tens of micrometers), the semi-infinite medium approximation can be considered. Equation related to the Fick's law equation was used to identify the change in oxygen concentration over time and depth due to solid-state diffusion [62]:

$$\frac{\partial c_i}{\partial t} = D\frac{\partial^2 c_i}{\partial x^2} \tag{1}$$

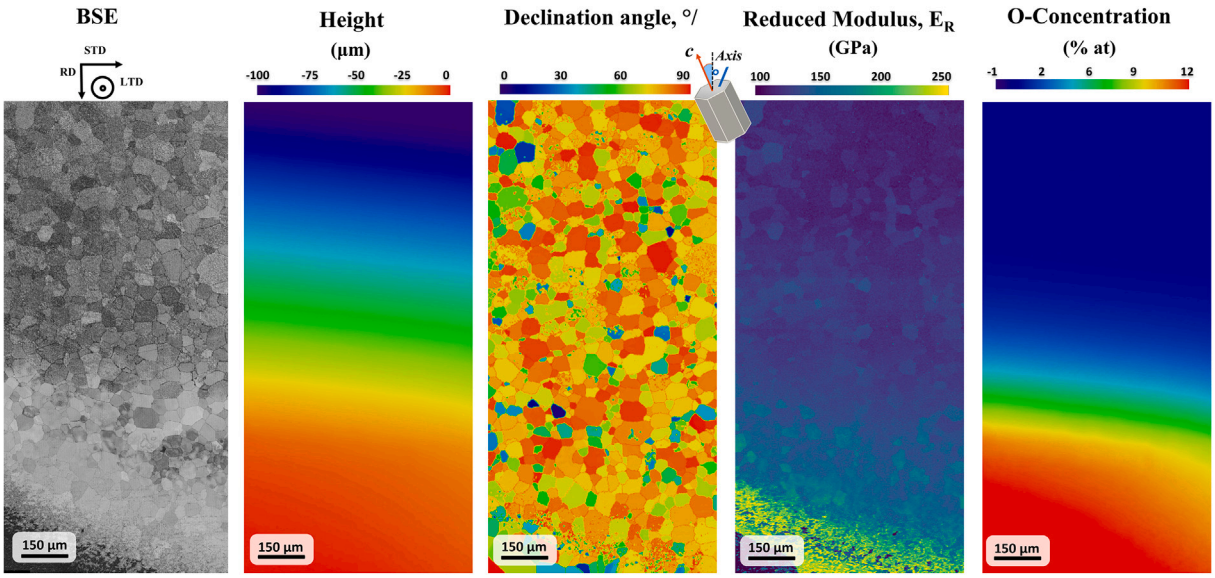

Fig. 5. Correlative mechanical microscopy applied to the heat-treated specimen at 855 °C : (a) BSE map, (b) Height map obtained by LSCM after rotation-correction, (c) Declination angle variation, (d) Elastic modulus variation, (e) Oxygen concentration variation computed from the height map.

where c_i is the concentration of the species i, D is the diffusion coefficient, t is time, and x is the distance to the metal/oxide interface. This law is used to explicitly identify the isotropic diffusion of oxygen in CP-Ti as a function of oxidation time, based on the experimentally identified diffusion profiles. In the case of diffusion in a semi-infinite solid, the oxygen distribution follows an erf-like function derived from Fick's law, as described in Eq. (2):

$$\frac{[O]_x - [O]_0}{[O]_s - [O]_0} = \frac{\Delta[O]_x}{\Delta[O]_{max}} = 1 - erf\left(\frac{x}{\sqrt{4 \cdot D_O^{Ti} \cdot t}}\right) \quad (2)$$

with a constant oxygen concentration at the metal/oxide interface $[O]_s$, a diffusion coefficient of O within Ti D_O^{Ti} independent of concentration and position, $[O]_x$ is the concentration of oxygen diffused at the position x after the time t, and $[O]_0$ is the oxygen concentration in the core of the sample, *i.e.*, the non-affected material. The maximal oxygen variation $\Delta[O]_{max}$ was considered here for direct comparison between relative oxygen concentration using EPMA or absolute oxygen concentration using HR-µLIBS. D_O^{Ti} and $[O]_s$ have been determined from EPMA and HR-µLIBS ($D_O^{Ti} = 1.9 \cdot 10^{-16}$ m^2.s^{-1} and $\Delta[O]_{max} = 11.5$ at. %). $[O]_0$ was measured HR-µLIBS (0.17 ± 0.09 at. %). The oxygen concentration at the metal/oxide interface is relatively low compared to the solubility limit (33 at% of O within Ti [8]) or the existing literature [11,13,35,63]. This point is further discussed in the manuscript.

3.2.1. Grain orientation and correlative mechanical microscopy

EBSD characterizations were conducted prior to high speed nanoindentation mapping (HSNM) to inform the local orientation of the grains in the region of interest on the wedge-cut surface. The declination angle is used here as the grain orientation descriptor (see Fig. 5)(c)). HSNM was then performed in order to determine the elastic anisotropy and its evolution as a function of the oxygen content through the reduced modulus modality. The individual response of the grains is clearly evidenced in Fig. 5(d), grains with a low declination angle have a much stiffer response at a given oxygen level. Based on the identified one-dimension diffusion profile, the sample topography of the wedge-cut sample using LSCM, the EBSD and HSNM maps, it is possible to register all the modalities in the HSNM modality (polynomial non-rigid registration) for multimodal correlative mechanical microscopy.

Table 2
Previous and revised sets of C_{ij} terms as a function of the oxygen concentration.

C_{ij} (GPa)	Previous parameters [53]	Revised parameters (This study)
C_{11}	$162.2\ (1+0.0645\Delta[O]^{0.45})$	$159.0\ (1+0.055\Delta[O]^{0.75})$
C_{12}	$91.8\ (1+0.04\Delta[O]^{0.65})$	$88.5\ (1+0.042\Delta[O]^{0.75})$
C_{13}	$68.8\ (1+0.07\Delta[O]^{0.65})$	$70.0\ (1+0.060\Delta[O]^{0.75})$
C_{33}	$180.5\ (1+0.055\Delta[O]^{0.9})$	$198.0\ (1+0.036\Delta[O]^{1.0})$
C_{44}	$46.7\ (1+0.15\Delta[O]^{0.65})$	$48.2\ (1+0.095\Delta[O]^{0.75})$
C_{66}	$0.5\ (C_{11}\text{-}C_{12})$	$0.5\ (C_{11}\text{-}C_{12})$

As for Ref. [53], the Vlassak and Nix model [54,55] was used to assess the evolution of the stiffness matrix as a function of the oxygen concentration based on the much more detailed and informative database obtained on the wedge-cut pre-oxidized sample. Identification of the C_{ij} terms as a function of the oxygen concentration was revised compared to Ref. [53]. Previous and revised sets of C_{ij} terms are summarized in Table 2.

The spatial dependence of the Young's modulus as a function of the oxygen concentration is illustrated in Fig. 6 in 2D and Fig. 7 in 3D for oxygen concentrations ranging between 0 at. % and 12 at. % based on the experimental oxygen profile characterization. The increase in elastic anisotropy, especially along the c-axis direction is still valid with the new set of C_{ij} parameters (Table 3). However, the evolution from the ovoid-shape function to the peanut-shape function is modified with the revised set of stiffness matrix terms when increasing the oxygen content (Fig. 7). The ovoid-shape function is more and more elongated along the a- and c-axis directions, but with a greater influence on the latter direction. Based on the isotropic transverse behavior of the spatial dependence of the Young's modulus, the representation of the spatial dependence of the Young's modulus in the c-/a-direction plane is sufficient. Therefore, the spatial dependence of the Young's modulus was thus depicted as a function of the oxygen concentration for the previous and new set of stiffness matrix parameters for direct and quantitative comparisons. While the evolution of the directional Young's modulus along the c-direction is very similar for both stiffness matrices, the evolution of the directional Young's modulus along the a-direction is prevalent for the new set of C_{ij} parameters (Fig. 6).

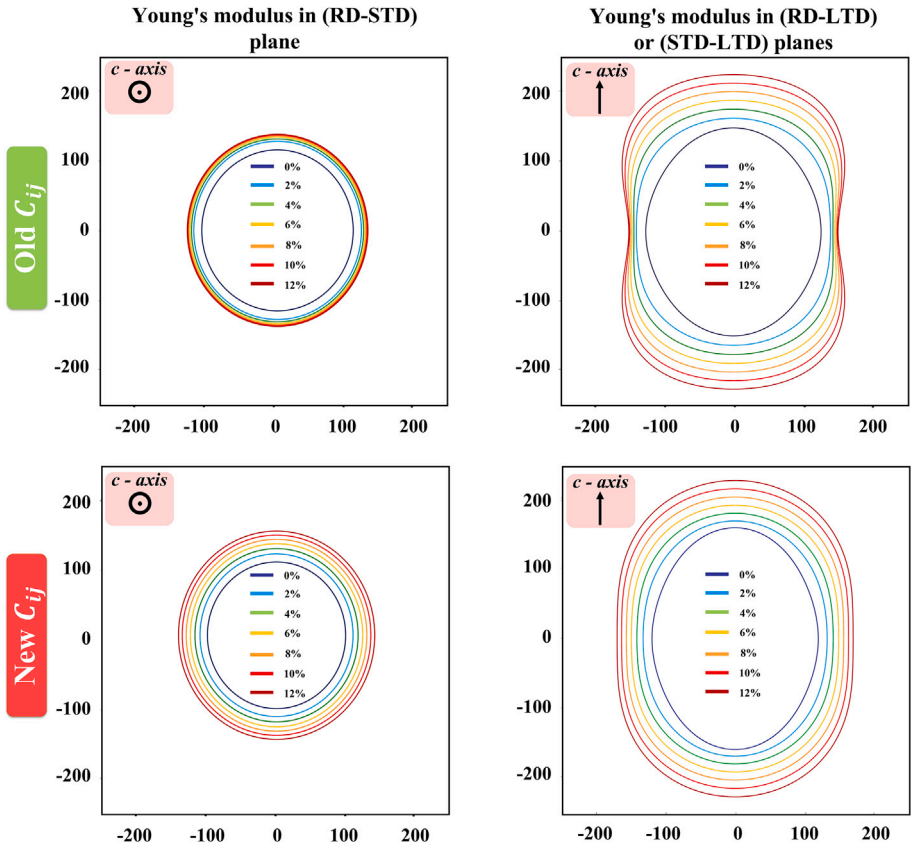

Fig. 6. Evolution of the spatial dependence of the Young's modulus (in GPa) in two dimensions (2D) as a function of the oxygen concentration (between 0 at. % and 12 at. %).

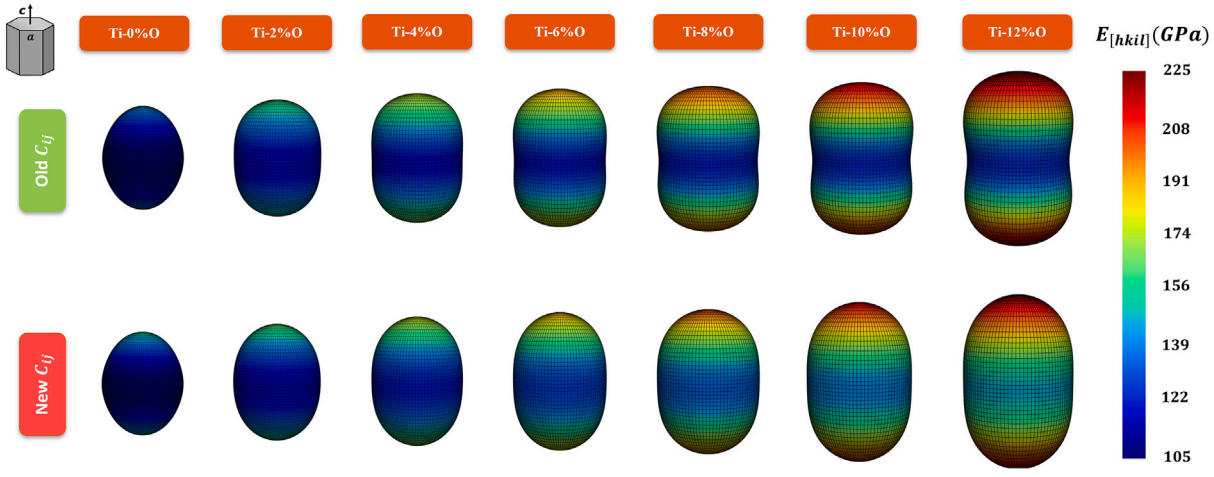

Fig. 7. Evolution of the spatial dependence of the Young's modulus in three dimensions (3D) as a function of the oxygen concentration (between 0 at % and 12 at %).

Table 3
Evolution of the terms of the stiffness matrix for CP-titanium with oxygen uptake. The anisotropy is characterized by the ratio $E_{[0001]}/E_{[01\bar{1}0]}$.

Composition	C_{11} (GPa)	C_{12} (GPa)	C_{13} (GPa)	C_{33} (GPa)	C_{44} (GPa)	C_{66}	$E_{[01\bar{1}0]}$ (GPa)	$E_{[0001]}$ (GPa)	Anisotropy
$Ti_{100}O_0$	159.00	88.50	70.00	198.00	48.20	35.25	103.98	158.4	1.523
$Ti_{98}O_2$	173.70	94.75	77.06	212.25	55.90	39.47	115.13	168.01	1.459
$Ti_{96}O_4$	183.73	99.01	81.87	226.51	61.15	42.36	122.88	179.09	1.457
$Ti_{94}O_6$	192.52	102.74	86.10	240.76	65.75	44.88	129.72	190.55	1.469
$Ti_{92}O_8$	200.59	106.18	89.97	255.02	69.98	47.20	136.04	202.24	1.487
$Ti_{90}O_{10}$	208.17	109.40	93.61	269.28	73.94	49.38	142	214.08	1.508
$Ti_{88}O_{12}$	215.38	112.46	97.07	283.53	77.72	51.45	147.68	226.04	1.531

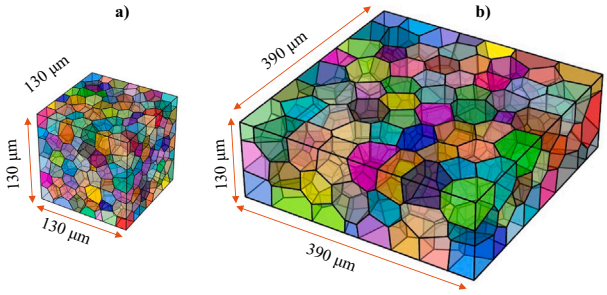

Fig. 8. Virtual polycrystalline sample generated via Neper, depicting a highly-equiaxed grain morphology, and a random orientation distribution (tessellation): (a) Grains tessellation for Ti as-received (400 grains for the FGA microstructure), (b) Grains tessellation for Ti as-received with the addition of the oxide layer, (c) Grains tessellation for Ti thermal-treated (200 grains for the CGA microstructure).

4. Finite element analysis

4.1. Numerical simulation framework

A 3D numerical simulation using finite elements was carried out on a polycrystalline aggregate to better understand the influence of the oxygen concentration gradient on the stress distribution at the sub-grain level of a pre-oxidized CP-Ti material in the elastic regime. In this study, the software Neper [64,65] was used to create virtual polycrystalline samples and the corresponding finite element mesh, allowing statistical control of grain size and shape distributions. To mitigate microstructural influences, parameters were chosen to generate samples with predominantly equiaxed grains. This specific morphology is achieved by the grain-growth morphology, with grains having a higher grain sphericities than in a Voronoi tesselation. This grain morphology more closely mimics the grain microstructure of the CP-Ti material. Two grain-size microstructures were considered to simulate the as-received material and the heat-treated material, as illustrated in Fig. 8.

To guarantee a sufficient statistical data set for each microstructure, fine-grain aggregates (FGA) with 400 grains for the as-received material with grain size of 20 ± 5 μm and coarse-grain aggregates (CGA) with 200 grains for heat-treated with grain size of 90 ± 5 μm were produced. The domain of the polycrystalline aggregate was defined as a parallelepiped of dimensions 130 × 130 × 130 μm^3 and 390 × 390 × 130 μm^3 for the FGA and CGA, respectively. It is worth mentioning that the grain orientations were kept similar for the different aggregates and were representative of the experimental texture of the CP-Ti material, as illustrated in Figs. 9 and 15.

In addition, the polycrystalline aggregates were also considered with and without a TiO_2 oxide layer onto the large face of the parallelepiped to also take into account the spallation capability of Ti and its influence on stress distribution at the sub-grain scale. The thickness of the oxide layer depends on the oxidation time and corresponds to one tenth of the oxygen-rich layer (ORL), as illustrated in Fig. 10.

Meshing of the aggregates was performed using Neper software [64,65] with the Gmsh command for tetrahedral meshing, a length set of 0.3 to enhance mesh refinement, as illustrated in Fig. 10.

The oxygen gradient within titanium, *i.e.*, the ORL, was also explicitly implemented using a Python script based on the identified erf-like function derived from Fick's law Eq. (2). Oxygen uptake is resolved as a function of oxidation time and thickness, as shown in Fig. 11. The ORL extension is taken as the depth at which oxygen uptake is of 0.5 at. %. The ORL extension for three different oxidation times at 650 °C were 20, 40 and 78 μm, respectively. The titanium based material was considered as an isotropic transverse elastic material with C_{ij} components varying as a function of the oxygen concentration (see the revised parameters in Table 2) and the external TiO_2 as an isotropic elastic material (E_{TiO_2} = 250 GPa, ν_{TiO_2} = 0.3) [66–68]. For numerical simulations, we used the open source software Zset [69,70], a finite element solver for multiphysics applications including crystal elasticity modeling based on the generalized Hooke's law ($\sigma_{ij} = C_{ijkl}\epsilon_{kl}$). Simple tension was applied to the aggregate. For that purpose, the displacement of the nodes of the left face (X = 0), normal to STD, is fixed to zero in the direction STD only. The displacement of the nodes of the back face (Y = 0), normal to RD, is fixed to zero in the direction RD only. The displacement of the nodes of the front face (Y = 1), normal to RD, is prescribed to a finite value in the direction RD. The displacement of the nodes of the bottom face (Z = 1), normal to LTD, is fixed to zero in the direction LTD only. In addition, the right face (X = 1) can deform but is constrained to remain flat. This corresponds to mixed homogeneous boundary conditions to prescribe an overall tensile loading. The names of the faces can be seen in Fig. 11.

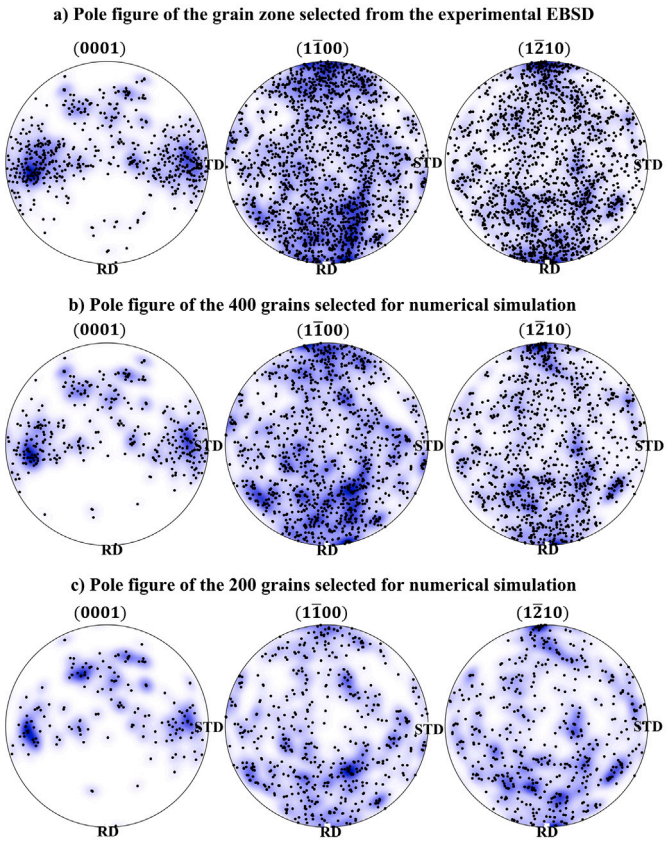

Fig. 9. Pole figures, depicting the crystallographic texture and orientation distribution of grains selected from the experimental EBSD data: (a) Pole figure generated on the basis of the mean values of the Euler angle of the grains in the selected zone, (b) 400 Grains texture (FGA), (c) 200 Grains texture (CGA).

4.2. Impact of the oxidation conditions on the stress heterogeneity of pre-oxidized Ti materials

Twelve different numerical simulations were carried out to depict differences in stress distribution within the oxygen-graded materials for 2 different grain-size microstructures, 3 oxidation times, and the occurrence or not of an adherent external oxide layer. Based on the different testing conditions, each simulation was labeled with a specific format "t = X h / YY ORL" or "t = X h / YY ORL + TiO_2", with "*X*" representing the oxidation duration prior to mechanical testing and "*YY*" the grain-size microstructure, *i.e.*, FG and CG for the fine-grain and coarse-grain microstructure, respectively. The "*ORL*" label corresponds to the testing

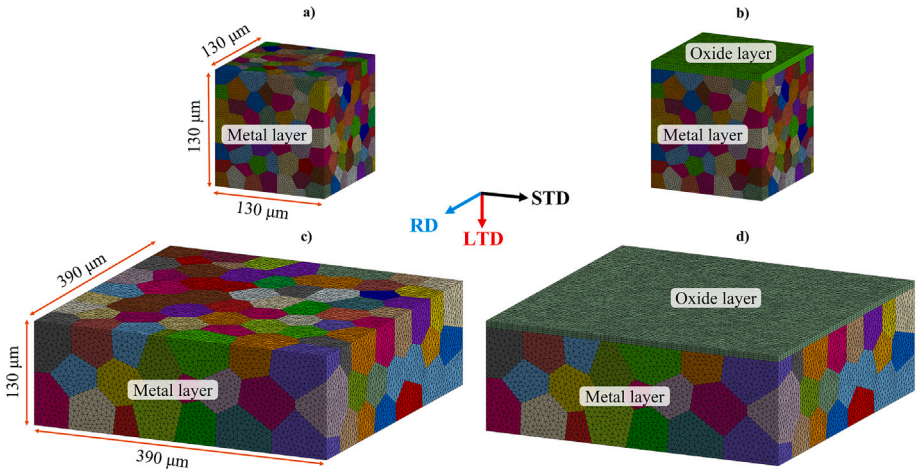

Fig. 10. Virtual polycrystalline sample meshing (length = 0.3)): (a) Grains tessellation for Ti as-received (400 grains), (b) Grains tessellation for Ti as-received (400 grains) with the addition of the oxide layer, (c) Grains tessellation for Ti thermal-treated (200 grains), (d) Grains tessellation for Ti thermal-treated with the addition of the oxide layer.

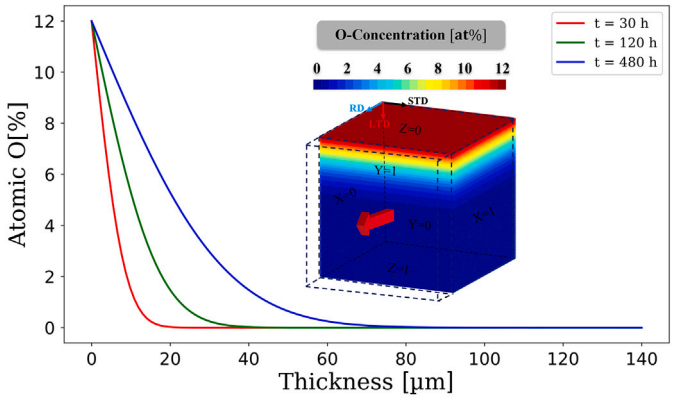

Fig. 11. Oxygen concentration as a function of thickness diffusion for 3 oxidation times and mechanical test prototype.

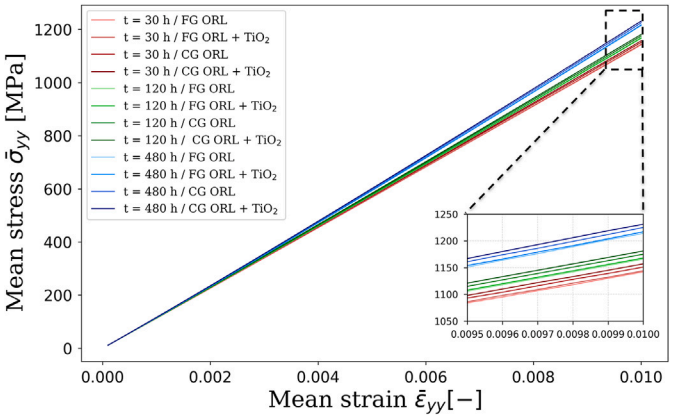

Fig. 12. Evolution of the averaged longitudinal stress σ_{yy} and strain ϵ_{yy}, y corresponding to the loading direction.

of the oxygen-graded aggregate in the absence of the external TiO_2 layer. Conversely, the "*ORL + TiO₂*" label corresponds to the testing of the oxygen-graded aggregate with the adherent external TiO_2 layer. Both the longitudinal stress σ_{yy} and strain ϵ_{yy} were averaged on the whole aggregate in order to simulate the macroscopic stress–strain curve for each simulation condition (Fig. 12). It is worth recalling that y corresponds to the macroscopic tensile loading direction. The pre-oxidation time was found to be the first-order parameter influencing the mechanical response. The longer the pre-oxidation time, the stiffer the oxygen-graded material. Interestingly, the grain size and the presence or not of the adherent external TiO_2 layer have no or little influence on the mechanical response. The lack of influence of the grain-size microstructure confirms that the number of grains in the polycrystalline aggregates was sufficient to capture the similar crystallographic texture.

The simulation results of the different polycrystalline aggregates are depicted in Figs. 13 and 14. The longitudinal stress component σ_{yy} is shown on the polycrystalline aggregates with the same color scale for all the tested conditions. The stress distribution appears particularly heterogeneous with greater values in the ORL due to its stiffer response. The stress at the surface (spalled oxide/bare surface) or the metal/oxide interface (adherent oxide) is 2.5 – 4 times greater than the macroscopic stress and slightly greater in the case of an adherent oxide scale. σ_{yy} reaches greater values in the volume for longer exposure time due to greater oxygen ingress. The longitudinal stress component σ_{yy} was also extracted for all the integration points of the O-rich surface for the aggregates deprived of TiO_2 or of the metal/oxide interface for the aggregates with TiO_2 (Figs. 13 and 14). Both locations experience maximal stresses compared to the volume and are of great importance to further explain the mechanical integrity of oxidizing components. The longitudinal stress component σ_{yy} was then normalized using the macroscopic longitudinal stress. The normalized stress distribution from this specific surface was reported on histograms to quantify both the average intensity and discrepancy in stress values compared to the averaged stress of the aggregate. Interestingly, the normalized longitudinal stress component σ_{yy} is greater for shorter oxidation time and exhibits a greater discrepancy, regardless of the presence of the external oxide or not. When comparing the normalized stress distribution at the specific surface in the presence of an oxide, the distribution appears to be more centered with a reduced discrepancy but a greater averaged value, which is expected due to the stiff isotropic elastic behavior considered for the oxide. In other words, these simulations demonstrated the particularly deleterious character of the oxygen ingress at the onset of the oxidation and more specifically in the case of an adherent oxide. This conclusion is very important based on the brittleness of the ORL. Similar results

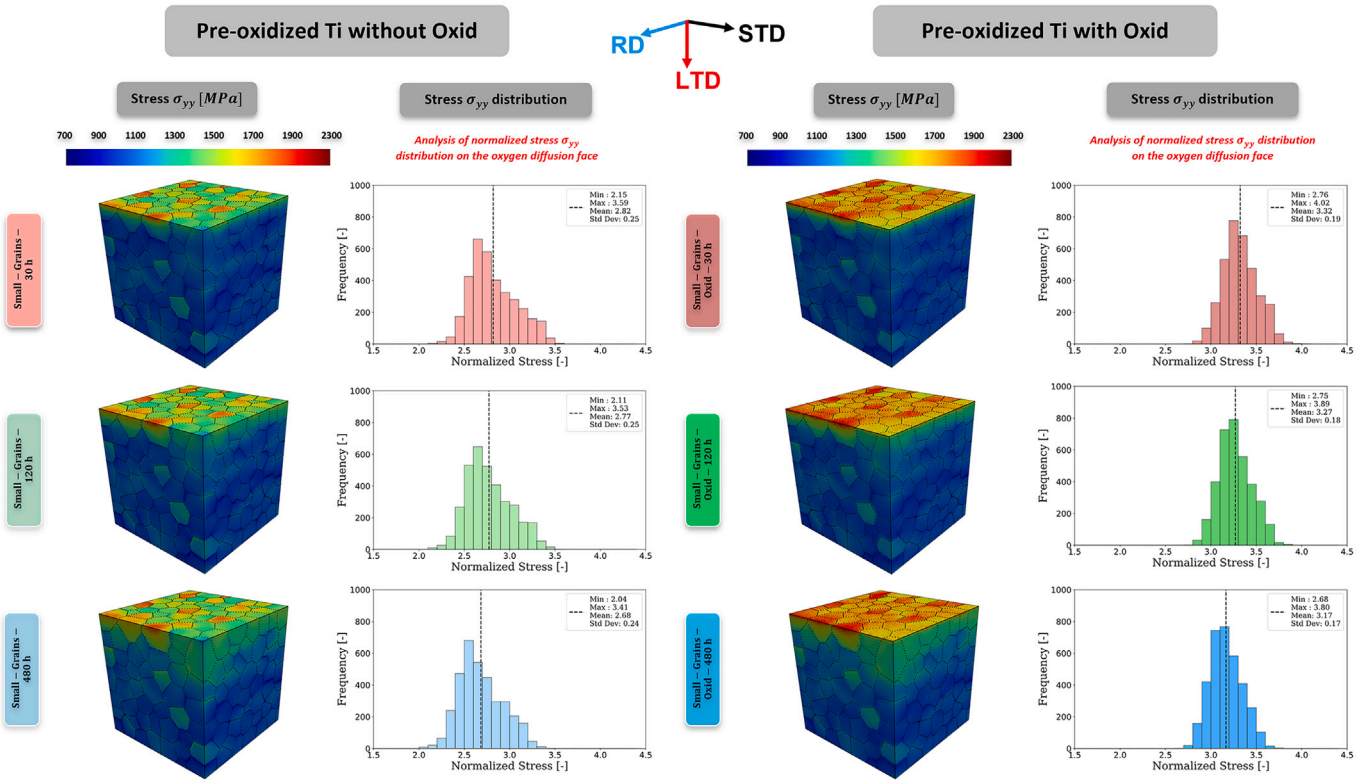

Fig. 13. Numerical results for as-received specimen (400 grains) with and without oxide layer (stress values are normalized by the mean macroscopic stress value).

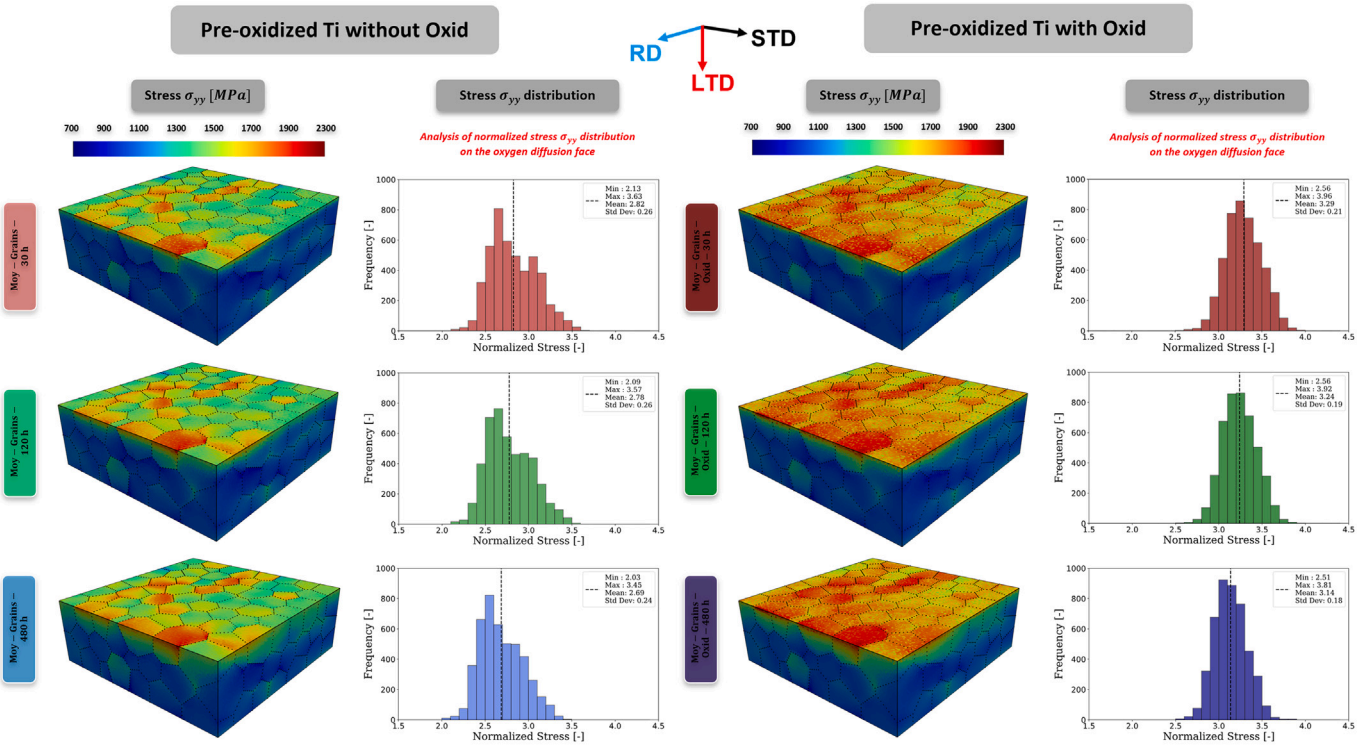

Fig. 14. Numerical results for the Ti thermal-treated (200 grains) specimen with and without oxide layer (stress values are normalized by the mean macroscopic stress value).

are obtained for both grain sizes. Additional simulations with different grain orientations, still representative of the experimental texture, are shown in Appendix. However, the present findings are similar for the different sets of grain orientations. The most striking result of the finite element simulations is that surface stresses up to 2.5 – 4 times greater than bulk stresses are induced by stiffnesses enhanced by a factor of 1.5 for high oxygen concentration according to Table 3. This is a consequence of grain to grain strain incompatibilities combined with oxygen concentration gradients.

4.3. Impact of oxygen diffusion and mechanical loading directions on the stress heterogeneity of pre-oxidized Ti materials

The studied CP-Ti material has a basal texture, *i.e.*, the *c*-direction being nearly aligned with STD. Therefore, the effect of both the diffusion direction and the mechanical loading direction on the anisotropic mechanical response of pre-oxidized titanium material was numerically tested using the same crystallographic texture and oxygen ingress (no oxide here). The texture information, *i.e.*, EBSD orientation maps, orientation distribution function, and declination angle map (°/), are depicted in the different directions of the rolling process in Fig. 15.

Six numerical simulations were performed, the oxygen diffusing along either STD, LTD, or RD, and the applied mechanical loading in both the directions perpendicular to that of oxygen diffusion, as shown in Fig. 16. The red and blue arrows of the coordinate systems correspond to the oxygen ingress and mechanical loading directions, respectively. Similar stress-state distribution analyses were performed to evaluate the mechanical heterogeneity at the oxidized surface. It is worth mentioning that the CP-Ti material has a nearly-basal texture (*c*-axis nearly aligned with STD) and have an isotropic transverse elastic behavior (α-Ti). In addition, the *c*-axis is nearly orthogonal to RD, the texture along the LTD being the less pronounced. Based on these texture directions, it appears normal that the displacement-imposed simulation leads to lower stress along RD and greater stress levels along STD, the stress level along LTD being intermediate. In addition, the nearly-basal texture leads to lower stress-distribution at the metal/oxide interface when applying tensile loading orthogonal to STD (*i.e.*, diffusion parallel to STD). Greater simulated volumes would improve the stress heterogeneity distribution due to some isolated grains leading to important stress concentration. Applying tensile loading along STD leads to greater average normalized stress at the metal/oxide interface due to the important increase in elastic anisotropy with oxygen addition, the Young's modulus along the *c*-axis being much stiffer with oxygen addition.

5. Discussion

The evolution of the elastic anisotropy of titanium with oxygen insertion was experimentally characterized using correlative mechanical microscopy, *i.e.*, high speed nanoindentation mapping (HSNM) paired with EBSD and both EPMA and HR-μLIBS. It is worth reminding that the HR-μLIBS demonstrated high throughput elemental analysis potential based on its measurement speed and quantitative composition assessment compared to EPMA analyses for a given sensitivity to oxygen, especially at very low oxygen concentrations (40 times faster). Gautier et al. [61] also compared diffusion profiles of oxygen in oxidized titanium showing the better resolution of HR-μLIBS in comparison to EPMA for the low oxygen contents (≤3 at. %). The particular use of wedge-cut preparation aimed to spread a 35 μm-deep ORL over 500 μm, to make all the characterization techniques more adequate to the spatial resolution of the ORL extension. The objective of this technique was to refine the terms of the stiffness matrix of titanium for different oxygen concentrations but also raised different questions that must be addressed. Several simulations of the oxygen-graded material for different oxidation exposures, oxidation conditions and grain sizes were performed and aimed to identify critical configuration leading to high stress concentration at the surface or at the metal/oxide interface, regions particularly brittle and with high stress concentration due to the stiffness increase with the oxygen content.

5.1. Wedge-cut preparation and oxygen ingress in titanium

Wedge-cut preparation consists in polishing the sample with a slight angle apart from the oxidized surface. Therefore, the normal direction of the surface of interest is nearly parallel to the oxygen flux during oxygen ingress. In comparison, conventional cross-section samples have their normal of surface of interest perpendicular to the oxygen flux. This point is particularly important since the crystallographic texture of the material, tested in terms of either mechanical or oxidation aspects, might play a role. In previous works on the nanoindentation response of CP-Ti materials [21,53], the surface of interest was chosen to offer the maximum amplitude of grain orientations to well capture the evolution of the hardness and reduced modulus as a function of the declination angle. Therefore, nanoindentation tests on pre-oxidized specimens were conducted on rolled plates in the LTD-STD plane, *i.e.*, the indentation direction and oxygen flux being parallel to the LTD and STD directions, respectively. The crystallographic texture is less pronounced in the LTD direction, offering a wide range of declination angles to be tested. However, based on the rolling process of thin CP-Ti plate, a strong basal texture is aligned along the STD direction (also called ND for normal direction in the literature), grains having mainly their *c*-axis aligned with the oxygen flux [71]. In the present investigation, the oxygen flux is along the LTD direction as well as the nanoindentation direction. Therefore, the relatively low oxygen content at the metal/oxide interface (nearly 12 at. % here) compared to the literature (nearly 20 – 25 at. % in Ref. [21,53] can find explanation in the crystallographic texture of the material at the oxidized surface, the formation of nitrides at the oxide/ORL interface, but also the oxidation temperature. As far as the effect of temperature is concerned, Jenkins [11] found that the temperature has a significant influence on the oxygen concentration at the metal/oxide interface. He reported that the oxygen concentration did not exceed 12 at% at 650 °C, 19 at% at 800 °C, and 25 at% at 900 °C. Similarly, Hurlen reported that oxygen is more soluble at an initial surface concentration of 14–15 at% than at higher concentrations due to the fact that Ti_6O is a more stable phase at the surface [63]. Initially, this latter compound exhibits superior properties compared to other oxides in the Ti-O system. In contrast, other researches indicated that the apparent solubility at the metal/oxide interface could reach up to 30 at%, especially at high temperatures (between 800 and 1200 °C) [13,25,72,73]. Unnam et al. [13] identified an oxygen concentration close to 20 at% at the metal/oxide interface for temperature ranging between 593 °C and 732 °C for a CP-Ti material but nearly 30 at% 760 °C, confirming the trend observed by Jenkins [11]. Based on the existing literature, the variation in oxygen concentration reported at the metal/oxide interface are highly dependent on the test conditions, *i.e.*, the temperature, the material, the surface texture and the atmosphere conditions. The formation of nitrides can also play a significant role on the oxygen concentration at the metal/oxide interface [16,17,19,24]. This point is not central here but can partly explain differences in oxygen concentration observed between Ref. [21,53] and the present study. Higher oxygen content at the metal/oxide interface would result in a stiffer ORL with increased elastic properties, that will be discussed in the following section.

In addition, Magazzeni et al. [21] reported a homogeneous distribution of oxygen within the ORL at a given distance from the metal/oxide interface using EPMA mapping on different grains. The question about the homogeneous/isotropic oxygen ingress remains open due to the explanation of the strong basal texture of the rolled plates, thus offering similar declination angle of grains to the oxygen ingress. Besides this, Chen et al. [74] demonstrated that titanium presents a slight

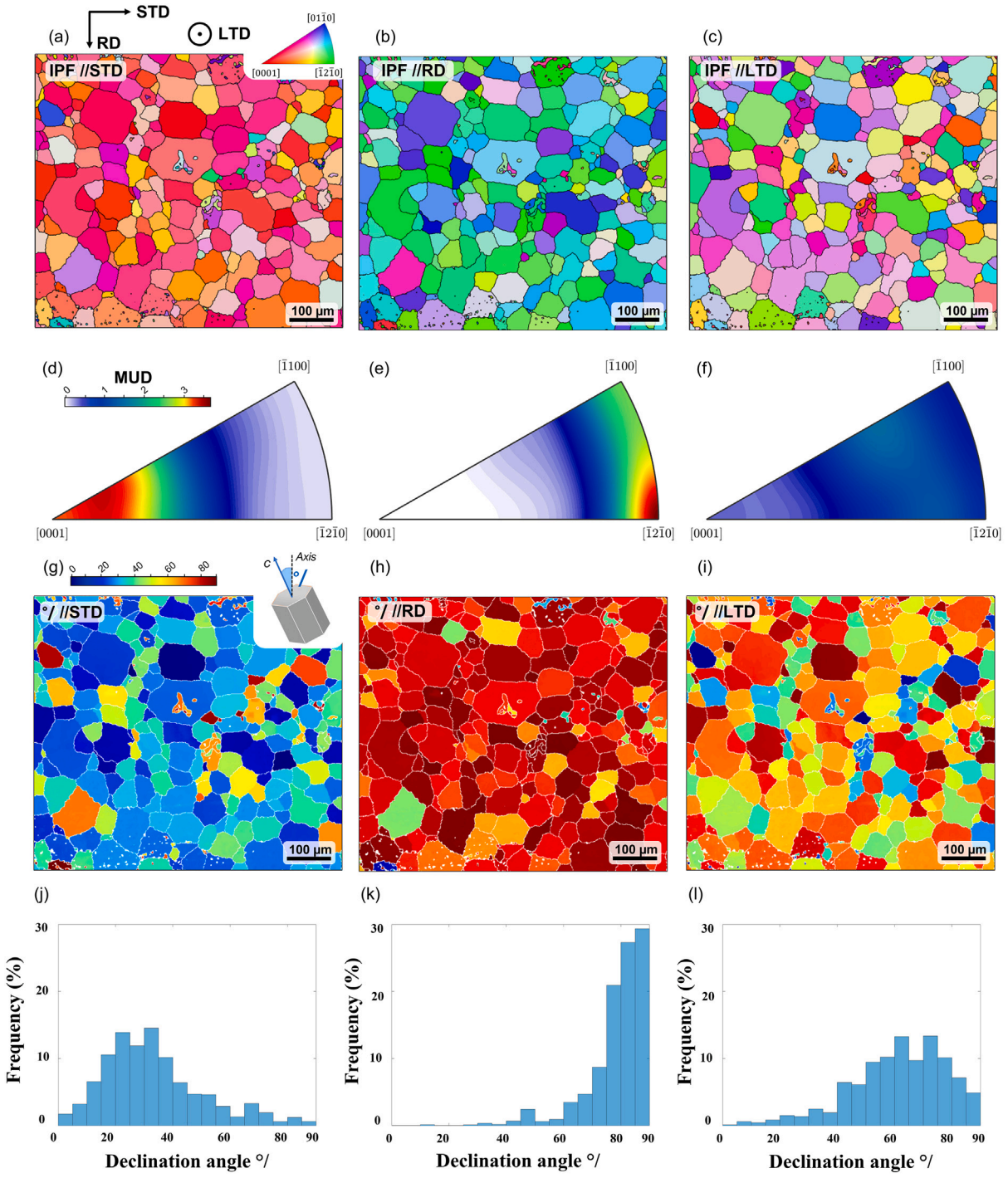

Fig. 15. Texture characterization of the CP-Ti after heat-treatment for selection of the plane to be tested by nanoindentation according to the different process directions, *i.e.*, STD, RD, LTD. (a-c) EBSD orientation maps, (d-f) Orientation distribution function represented on an IPF with a maximal multiple of uniform density of 3.7, (g-i) Declination angle map (°/), (j-l) Distribution function of the declination angle.

oxidation anisotropy due to its adsorption behavior and diffusion process of oxygen atoms on surfaces with different crystal orientations. They demonstrated that (0001) surfaces has higher adsorption energy and stronger diffusion barrier than the (0110) surfaces, which can better resist oxygen attack. Therefore, grains with an orientation close to ⟨0001⟩ are expected to have a lower oxidation rate and a better oxidation resistance. In addition, Wu et al. [14,15] performed ab-initio simulations and found a slight anisotropic diffusivity of O within Ti, and that other chemical elements can favor or not this diffusivity. While the texture of the material at the oxidized surface is weak in the present study, the oxygen content was assumed homogeneous at a given depth from the metal/oxide interface (isotropic diffusion), as commonly reported in the literature. The anisotropic oxidation and oxygen ingress of titanium could be considered in further studies using adapted characterization techniques to improve the multi-modality of the correlative mechanical microscopy.

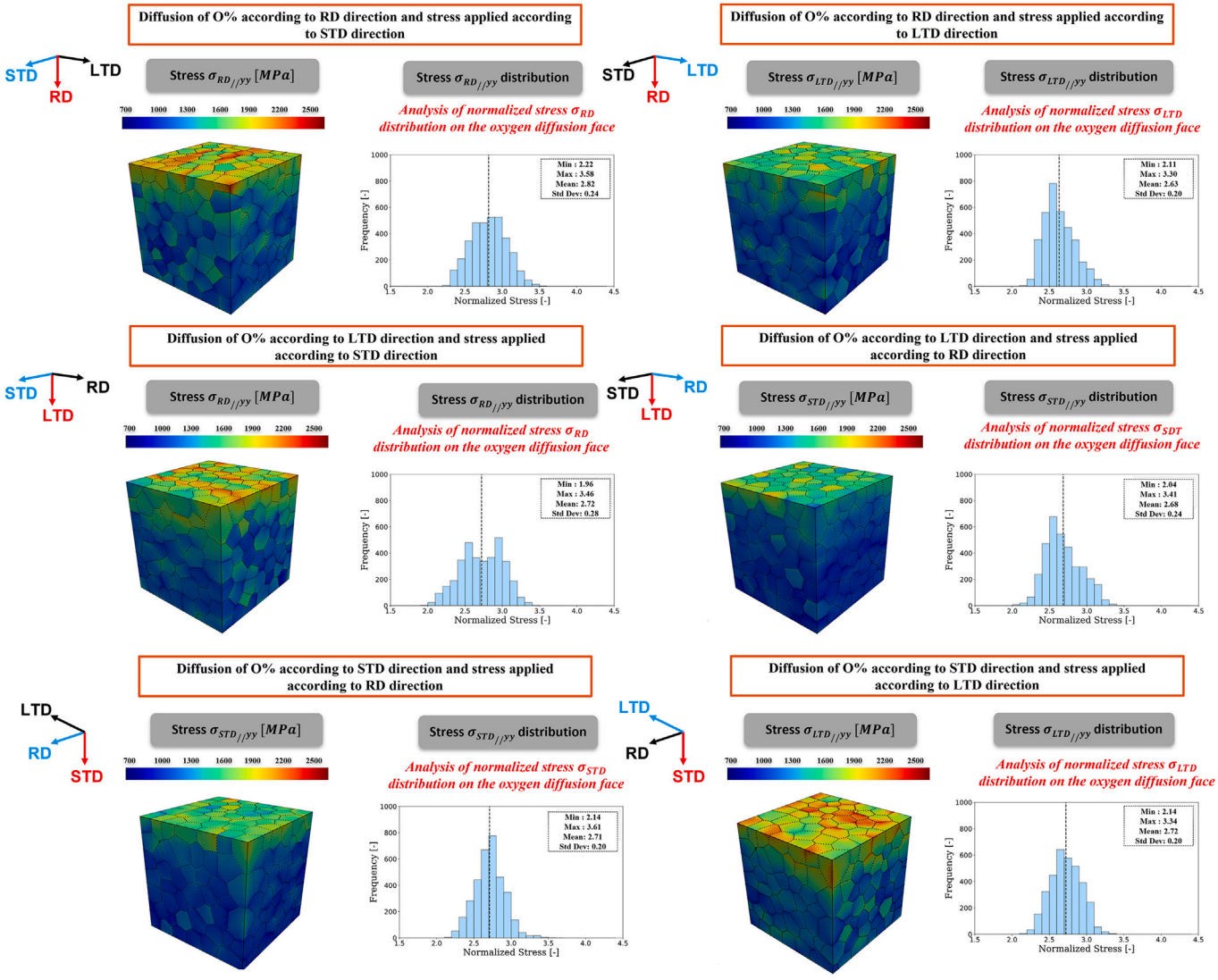

Fig. 16. Numerical modeling results for oxygen diffusion in different directions and different mechanical loading directions.

5.2. The effect of the oxygen ingress and change in elastic properties on the mechanical response of the pre-oxidized polycrystalline aggregates

Despite the oxygen strengthening effect, the ORL is extremely brittle and its mechanical integrity is of high importance for titanium-based structural components exposed to high temperatures. Therefore, identifying the local mechanical behavior at the ORL scale and simulating the mechanical response of the oxygen-graded material can shed light on critical configurations of microstructural features leading to intense stress concentration. As aforementioned, the use of the wedge-cut technique aimed at improving the determination of the stiffness matrix as a function of the oxygen concentration due to increase in spatial description of the oxygen very rich-layer. It is worth mentioning that oxygen insertion is accompanied with internal stresses, which are neglected in the present inverse simulation work. The hardness properties are more significantly affected by internal stresses than elastic properties. However, this point deserves more investigation when measuring elastic properties from the dynamic response of the material, as for CSM indentation. Previous works evidenced interesting size effects of pre-oxidized titanium-based alloys with different thickness and oxygen ingress using one-dimension simulation of an oxygen-graded titanium alloy [44].

It was reported that short oxidation times or thicker specimens for a given oxidation time would result in greater stress at the surface. This core/shell result is in line with the present three-dimensional finite element simulations. However, the third dimension, the polycrystalline aggregate and the anisotropic elastic evolution as a function of oxygen can be included in the numerical framework to simulate different elastic behaviors. The originality in the present numerical work was to highlight (1) the role of the external oxide on the increase in average stress level at the metal/oxide interface compared to a bare sample with an ORL, (2) greater stress level at the metal/oxide interface or the bare ORL surface for short oxidation times (or thick samples based on the lack of internal length in such elastic calculations), (3) the greater discrepancy in stress at the metal/oxide interface or the bare ORL surface for short oxidation times. These findings are observed for different sets of crystallographic orientations, the intensity in stress being orientation dependent. Such size/short-term exposure tendencies demonstrate that the onset of oxidation is detrimental for the mechanical integrity of pre-oxidized components, suggesting a high sensitivity to mechanochemical coupling due to increased stress concentrations. A competition between ORL extension and maximal stresses would require additional characterizations to better predict the competition between

oxygen strengthening and embrittlement reported in Ref. [35] on ultrathin specimens with ORL being in the same order of the specimen thicknesses.

As aforementioned, the concentration at the metal/oxide interface can significantly vary depending on the pre-oxidation temperature but also the material crystallographic and the atmospheric conditions. However, a richer ORL in oxygen is prone to a stiffer response. Despite the richer region in oxygen might occupy nearly 10 % of the ORL, richer oxygen content would increase both the normalized longitudinal stress component σ_{yy} at the specimen surface or metal/oxide interface and the discrepancy in stress response at this specific surface. These latter points are particularly important to evaluate the mechanical integrity of pre-oxidized components, especially as a function of their crystallographic texture. Both numerical and experimental characterizations similar to Ref. [35,44] would be beneficial to elucidate the role of the crystallographic texture on the oxygen embrittlement sensitivity.

6. Conclusions

The present paper proposes a numerical and experimental framework to better identify the change in anisotropic elastic properties of titanium with different oxygen contents and simulate the mechanical response of an oxygen-graded material corresponding to the case of a pre-oxidized Ti specimen. The different conclusions of the present work can be summarized as:

- The use of wedge-cut sample aimed at extending the spatial distribution of the ORL compared to conventional cross-section samples, improving the determination of the spatial dependence of the Young's modulus as a function of the oxygen content, *i.e.*, the elastic anisotropy of the material for different oxygen contents;
- Both EPMA and HR-μLIBS analyses revealed similar oxygen profiles in the pre-oxidized titanium, the HR-μLIBS analysis yet providing absolute oxygen concentration as low as 100 ppm at. while the EPMA results are relative to the bulk concentration due to inevitable surface contamination. It is worth mentioning that the measurement acquisition time per spot analysis was of 2 s and 0.05 s for the EPMA and HR-μLIBS analyses, respectively (oxygen concentration profiles of 54 h with EPMA versus 1.4 h with HR-μLIBS for similar spatial resolution and sensitivity);
- Grain to grain strain incompatibilities were found to enhance surface stress concentration induced by the gradient of elastic stiffness.
- The finite element simulations of a polycrystalline aggregate aimed to test different sets of crystallographic orientations with different ORL extensions. The short oxidation exposure was found particularly detrimental for the mechanical integrity of titanium-based materials due to greater average stresses but also maximal values;
- The presence of an adherent TiO_2 oxide induced greater stress concentration at the metal/oxide interface for a given pre-oxidation condition compared to a bare material with the same ORL.
- From the modelling perspective, a missing aspect of the presented anisotropic elasticity simulations is the consideration of the eigenstrain depending on the oxygen concentration. This consideration, combined with stress-gradient-induced oxygen diffusion, will be the subject of future work to revisit the evolution of stress distribution in the ORL. The obtained stress levels also plead for the introduction of crystal plasticity effects in the computational analysis.

7. License

This research was funded, in whole or in part, by The European Research Council, project HT-S_4DefOx - Grant number 948,007. A [CC-BY public copyright license] has been applied by the authors to the present document and will be applied to all subsequent versions up to the Author Accepted Manuscript arising from this submission, in accordance with the grant's open access conditions.

CRediT authorship contribution statement

Ayyoub Dziri: Writing – original draft, Visualization, Software, Methodology, Investigation, Formal analysis, Data curation. **Kais Ammar:** Writing – review & editing, Visualization, Methodology, Investigation, Conceptualization. **Samuel Forest:** Writing – review & editing, Validation, Supervision, Conceptualization. **Henry Proudhon:** Writing – review & editing, Conceptualization. **Quentin Sirvin:** Writing – review & editing, Visualization, Methodology, Investigation, Data curation. **Thiebaud Richeton:** Writing – review & editing, Software. **Damien Texier:** Writing – original draft, Visualization, Validation, Supervision, Resources, Project administration, Methodology, Investigation, Funding acquisition, Conceptualization.

Declaration of competing interest

The authors declare the following financial interests/personal relationships which may be considered as potential competing interests:

Damien TEXIER reports that financial support was provided by European Research Council. If there are other authors, they declare that they have no known competing financial interests or personal relationships that could have appeared to influence the work reported in this paper.

Acknowledgements

The authors are particularly grateful to Antoine CASADEBAIGT and François FARIAUT from LASALYS and Sophie GOUY from Raimond Castaing Microanalysis Centre (UAR 3623) for performing HR-μLIBS analyses and EPMA analyses, respectively. The authors would like to thank Daniel MONCEAU and Kévin GAUTIER from CIRIMAT for providing standards for the calibration curve of the HR-μLIBS analyses with the specific parameters. This work was supported by the European Research Council [project HT-S_4DefOx - Grant number 948007].

Appendix A

As mentioned in the manuscript, different sets of crystal orientations were tested and the simulation results are shown in Figs. 17–19. Observed trends are similar to those described in the manuscript regardless of the crystallographic texture of the polycrystalline aggregate (orientations randomly distributed from the 400 grains and 200 grains texture) when considering isotropic oxygen diffusion: (1) Shorter oxidation exposure leads to greater average longitudinal stresses and stress amplitude, (2) An adherent TiO_2 oxide induced greater stress concentration at the metal/oxide interface for a given pre-oxidation condition compared to a bare material with the same ORL.

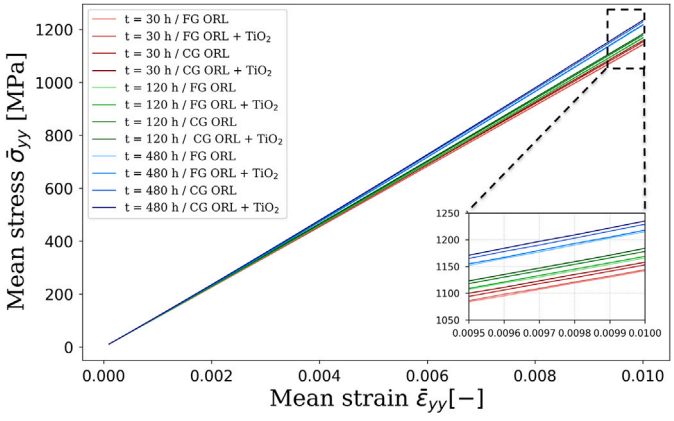

Fig. 17. Variation of elastic stress in y direction with strain for a second random distribution of Euler angles of grains.

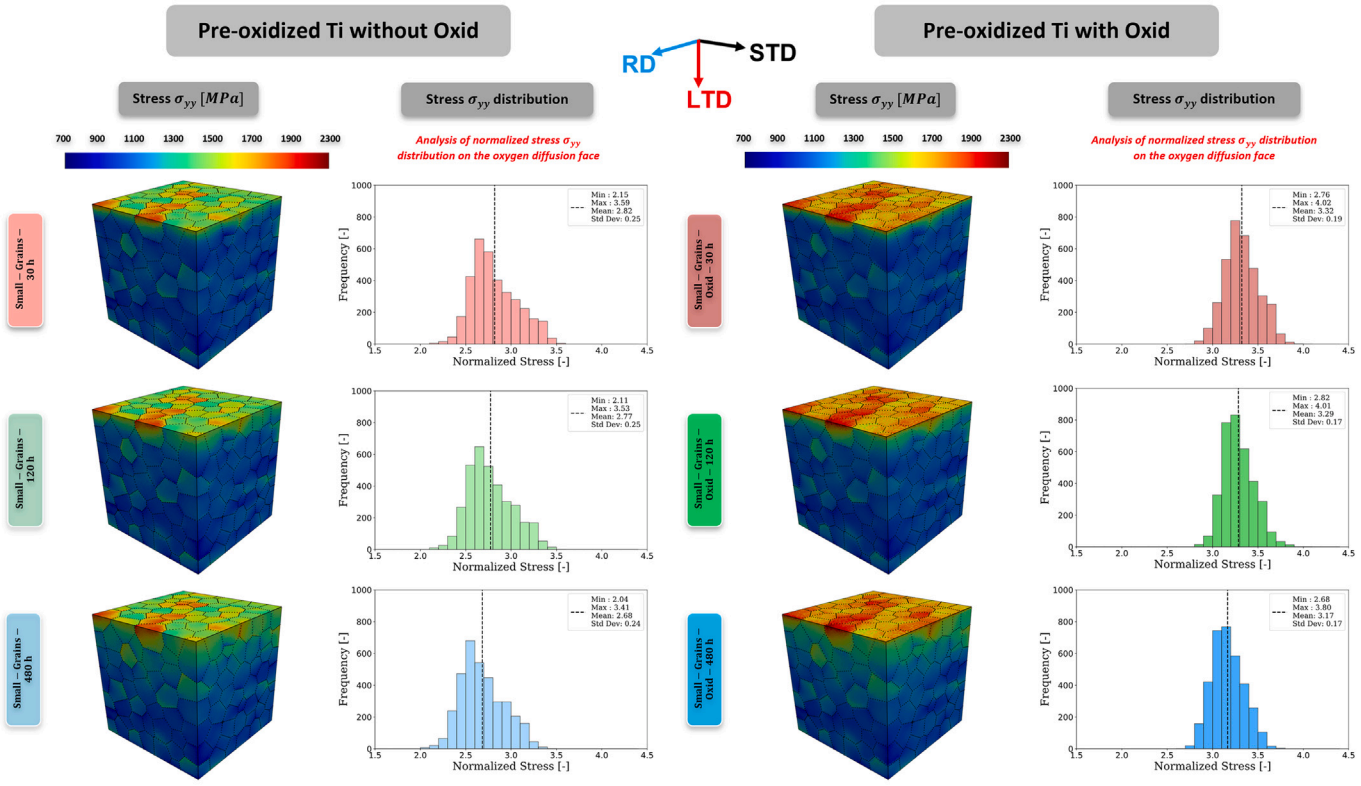

Fig. 18. Numerical results for as-received specimen (400 grains) with and without oxide layer (stress values are normalised by the mean macroscopic stress value).

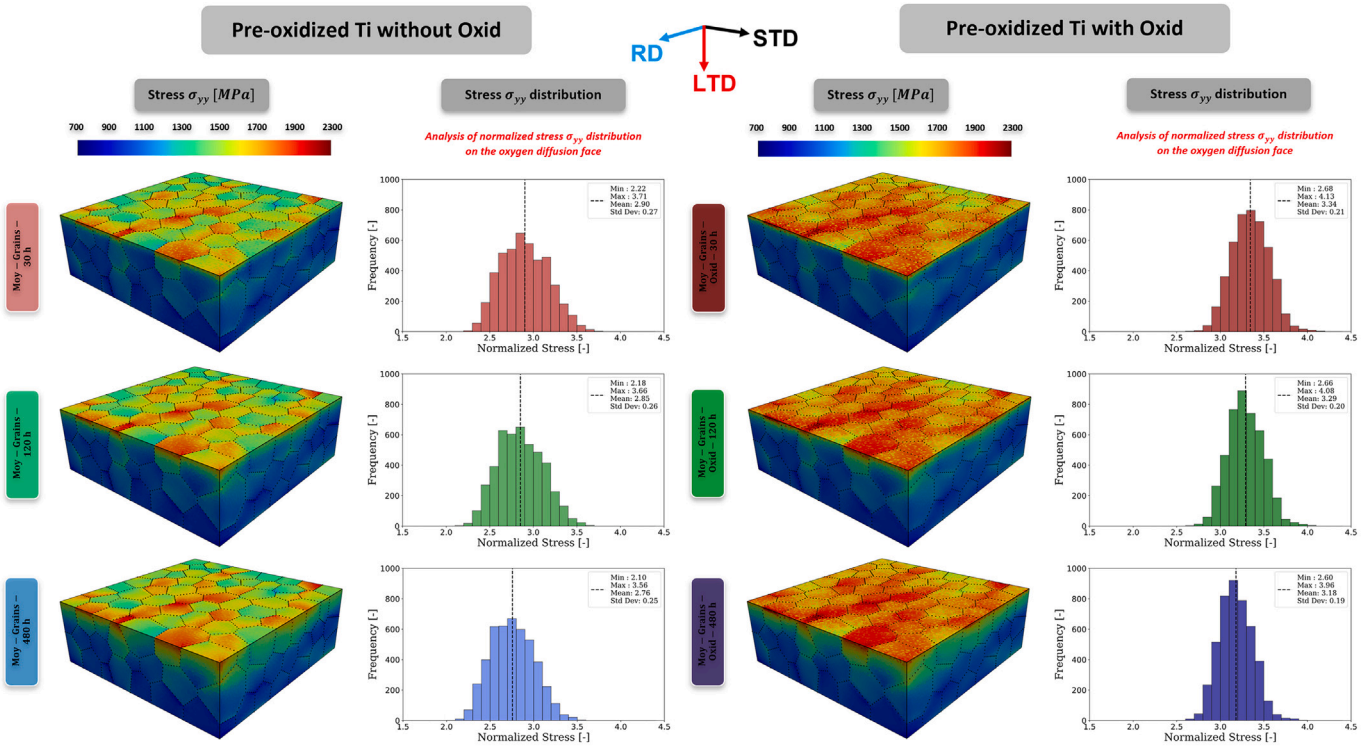

Fig. 19. Numerical results for the Ti thermal-treated (200 grains) specimen with and without oxide layer (stress values are normalised by the mean macroscopic stress value).

Appendix B. Supplementary data

Supplementary data to this article can be found online at doi:10.1016/j.matdes.2025.114801.

Data availability

Data will be made available on request.

References

[1] M. Peters, J. Kumpfert, C.H. Ward, C. Leyens, Titanium alloys for aerospace applications, Adv. Eng. Mater. 5 (2003) 419–427, https://doi.org/10.1002/adem.200310095

[2] J.C. Williams, R.R. Boyer, Opportunities and issues in the application of titanium alloys for aerospace components, Metals 10 (2020) 705, https://doi.org/10.3390/met10060705

[3] D. Banerjee, J.C. Williams, Perspectives on titanium science and technology, Acta Materialia 61 (2013) 844–879, https://doi.org/10.1016/j.actamat.2012.10.043

[4] C.N. Elias, J.H.C. Lima, R.Z. Valiev, M.A. Meyers, Biomedical applications of titanium and its alloys, JOM 60 (2008) 46–49, https://doi.org/10.1007/s11837-008-0031-1

[5] V.V. Larionov, V.A. Varlachev, X. Shupeng, Accumulation of hydrogen in titanium exposed to neutron irradiation, Int. J. Hydrog. Energy 45 (2020) 15294–15301, https://doi.org/10.1016/j.ijhydene.2020.04.014

[6] P.K. Kofstad, High Temperature Corrosion, Elsevier Applied Science, 1988, https://doi.org/10.1002/maco.19880390713

[7] G. Lütjering, J.C. Williams, Titanium, Engineering Materials and Processes, Springer Berlin Heidelberg, 2007, https://doi.org/10.1007/978-3-540-73036-1

[8] J.L. Murray, H.A. Wriedt, The o-ti (oxygen-titanium) system, J. Phase Equilib. 8 (1987) 148–165, https://doi.org/10.1007/BF02873201

[9] D. David, E.A. Garcia, X. Lucas, G. Beranger, Etude de la diffusion de l'oxygène dans le titaneα oxydé entre 700 °c et950 °c, J. Less-Common Met. 65 (1979) 51–69, https://doi.org/10.1016/0022-5088(79)90152-8

[10] J. Liu, X. Fan, C. Sun, W. Zhu, Oxidation of the titanium (0001) surface: diffusion processes of oxygen from DFT, RSC Adv. 6 (2016) 71311–71318, https://doi.org/10.1039/C6RA13877B

[11] A. Jenkins, The oxidation of titanium at high temperatures in an atmosphere of pure oxygen, J. Inst. Met. 82 (1954) https://doi.org/10.1016/S0042-207X(54)80169-2

[12] T. Hurlen, H. Kjöllesdal, J. Markali, N. Norman, Oxidation of Titanium, Central Institute for Industrial Research, 1958.

[13] J. Unnam, R.N. Shenoy, R.K. Clark, Oxidation of commercial purity titanium, Oxid. Met. 26 (1986) 231–252, https://doi.org/10.1007/BF00659186

[14] H.H. Wu, D.R. Trinkle, Direct diffusion through interpenetrating networks: oxygen in titanium, Phys. Rev. Lett. 107 (2011) 045504, https://doi.org/10.1103/PhysRevLett.107.045504

[15] H.H. Wu, D.R. Trinkle, Solute effect on oxygen diffusion inα-titanium, J. Appl. Phys. 113 (2013) 223504, https://doi.org/10.1063/1.4808283

[16] I. Abdallah, C. Dupressoire, L. Laffont, D. Monceau, A. Vande Put, STEM-EELS identification of TiO_xN_y, TiN, Ti_2N and O, N dissolution in the Ti2642s alloy oxidized in synthetic air at 650 °C, Corros. Sci. 153 (2019) 191–199, https://doi.org/10.1016/j.corsci.2019.03.037

[17] C. Dupressoire, M. Descoins, A. Vande Put, E. Epifano, D. Mangelinck, P. Emile, D. Monceau, The role of nitrogen in the oxidation behaviour of a Ti6242s alloy: a nanoscale investigation by atom probe tomography, Acta Materialia 216 (2021) 117134, https://doi.org/10.1016/j.actamat.2021.117134

[18] T.C. Valenza, P.K. Weber, E.A. Marquis, Role of nitrogen in the high-temperature oxidation of titanium alloys, Corros. Sci. 235 (2024) 112164, https://doi.org/10.1016/j.corsci.2024.112164

[19] K. Gautier, D. Monceau, E. Epifano, D. Connétable, T. Gheno, Study of the role of nitrogen in the oxidation of titanium-based alloys by changing the reaction gas, High Temp. Corros. Mater. 101 (2024) 861–872, https://doi.org/10.1007/s11085-024-10275-6

[20] D. Connétable, R. Besson, K. Gautier, E. Epifano, D. Monceau, First-principles study of point defects in TI–N compounds including oxygen insertion – consequences on oxidation of ti alloys, J. Phys. Chem. C 128 (2024) 14477–14499, https://doi.org/10.1021/acs.jpcc.4c03727

[21] C.M. Magazzeni, H.M. Gardner, I. Howe, P. Gopon, J.C. Waite, D. Rugg, D.E.J. Armstrong, A.J. Wilkinson, Nanoindentation in multi-modal map combinations: a correlative approach to local mechanical property assessment, J. Mater. Res. 36 (2020) 2235–2250, https://doi.org/10.1557/s43578-020-00035-y

[22] N. Vaché, Y. Cadoret, B.B. Dod, D. Monceau, Modeling the oxidation kinetics of titanium alloys: review, method and application to Ti-64 and Ti-6242s alloys, Corros. Sci. 178 (2021) 109041, https://doi.org/10.1016/j.corsci.2020.109041

[23] J. Baillieux, D. Poquillon, B. Malard, Relationship between the volume of the unit cell of hexagonal-close-packed Ti, hardness and oxygen content after α-case formation in Ti-6Al-2Sn-4Zr-2Mo-0.1Si alloy, J. Appl. Crystallogr. 49 (2016) 175–181, https://doi.org/10.1107/S1600576715022906

[24] K. Cavé, D. Texier, S. Vallot, N. Chanfreau, E. Fessler, M. Dehmas, D. Monceau, D. Poquillon, Effect of creep loading on the oxygen diffusion of ti6242s at 650°C, Scripta Mater. 238 (2024) 115748, https://doi.org/10.1016/j.scriptamat.2023.115748

[25] K. Wiedemann, R. Shenoy, J. Unnam, Microhardness and lattice parameter calibrations of the oxygen solid solutions of unalloyed α-titanium and ti-6al-2sn-4zr-2mo, Metall. Trans. A 18 (1987) 1503–1510, https://doi.org/10.1007/BF02646662

[26] F.B. Kværndrup, Ö.C. Kücükyildiz, G. Winther, M.A.J. Somers, T.L. Christiansen, Extreme hardening of titanium with colossal interstitial contents of nitrogen and oxygen, Mater. Sci. Eng. A 813 (2021) 141033, https://doi.org/10.1016/j.msea.2021.141033

[27] B. Barkia, V. Doquet, J.P. Couzinié, I. Guillot, E. Héripré, In situ monitoring of the deformation mechanisms in titanium with different oxygen contents, Mater. Sci. Eng. A 636 (2015) 91–102, https://doi.org/10.1016/j.msea.2015.03.044

[28] W.L. Finlay, J.A. Snyder, Effects of three interstitial solutes (nitrogen, oxygen, and carbon) on the mechanical properties of high-purity, alpha titanium, JOM 2 (1950) 277–286, https://doi.org/10.1007/BF03399001

[29] H. Conrad, Effect of interstitial solutes on the strength and ductility of titanium, Prog. Mater. Sci. 26 (1981) 123–403, https://doi.org/10.1016/0079-6425(81)90001-3

[30] F. Amann, R. Poulain, S. Delannoy, J.-P. Couzinie, E. Clouet, I. Guillot, F. Prima, An improved combination of tensile strength and ductility in titanium alloys via oxygen ordering, Mater. Sci. Eng. A 867 (2023) 144720, https://doi.org/10.1016/j.msea.2023.144720

[31] H. Hornberger, C. Randow, C. Fleck, Fatigue and surface structure of titanium after oxygen diffusion hardening, Mater. Sci. Eng. A 630 (2015) 51–57, https://doi.org/10.1016/j.msea.2015.02.006

[32] A.A. Hidalgo, T. Ebel, W. Limberg, F. Pyczak, Influence of oxygen on the fatigue behaviour of Ti-6Al-7Nb alloy, Key Eng. Mater. 704 (2016) 44–52, https://doi.org/10.4028/www.scientific.net/KEM.704.44

[33] D.P. Satko, J.B. Shaffer, J.S. Tiley, S.L. Semiatin, A.L. Pilchak, S.R. Kalidindi, Y. Kosaka, M.G. Glavicic, A.A. Salem, Effect of microstructure on oxygen rich layer evolution and its impact on fatigue life during high-temperature application of α/β titanium, Acta Mater. 107 (2016) 377–389, https://doi.org/10.1016/j.actamat.2016.01.058

[34] Q. Sirvin, D. Texier, V. Velay, D. Monceau, B. Dod, Oxygen content effect on mechanical behaviour of cp titanium exposed at elevated temperature., in: Issu De Proceedings of the 15th World Conference on Titanium, vol. Chapter 12: Environmental Applications, Edinburgh, United Kingdom, 2023, pp. 6, https://doi.org/10.7490/f1000research.1119895.1

[35] Q. Sirvin, J. Genée, B. Dod, D. Monceau, D. Texier, Oxygen ingress in titanium and its alloys after high temperature oxidation: a competition between strengthening and embrittlement, Metall. Trans. A 56 (2025) 1858–1874, https://doi.org/10.1007/s11661-025-07737-0

[36] J.M. Oh, B.G. Lee, S.W. Cho, S.W. Lee, G.S. Choi, J.W. Lim, Oxygen effects on the mechanical properties and lattice strain of Ti and Ti-6Al-4V, Metals Mater. Int. 17 (2011) 733–736, https://doi.org/10.1007/s12540-011-1006-2

[37] B. Sun, S. Li, H. Imai, T. Mimoto, J. Umeda, K. Kondoh, Fabrication of high-strength ti materials by in-process solid solution strengthening of oxygen via P/M methods, Mater. Sci. Eng. A 563 (2013) 95–100, https://doi.org/10.1016/j.msea.2012.11.058

[38] M.L. Wasz, F.R. Brotzen, R.B. Mclellan, A.J. Griffin, Effect of oxygen and hydrogen on mechanical properties of commercial purity titanium, Int. Mater. Rev. 41 (1996) 1–12, https://doi.org/10.1179/imr.1996.41.1.1

[39] L. Bendersky, A. Rosen, The effect of exposure on the mechanical properties of the Ti-6Al-4V alloy, Eng. Fract. Mech. 20 (1984) 303–311, https://doi.org/10.1016/0013-7944(84)90135-8

[40] R.N. Shenoy, J. Unnam, R.K. Clark, Oxidation and embrittlement of Ti-6Al-2Sn-4Zr-2Mo alloy, Oxid. Met. 26 (1986) 105–124, https://doi.org/10.1007/BF00664276

[41] J.M. Oh, B.G. Lee, S.-W. Cho, S.-W. Lee, G.-S. Choi, J.-W. Lim, Oxygen effects on the mechanical properties and lattice strain of Ti and Ti-6Al-4V, Metals Mater. Int. 17 (2011) 733–736, https://doi.org/10.1007/s12540-011-1006-2

[42] N. Vaché, D. Monceau, Oxygen diffusion modeling in titanium alloys: new elements on the analysis of microhardness profiles, Oxid. Met. 93 (2020) 215–227, https://doi.org/10.1007/s11085-020-09956-9

[43] Z. Cai, T. Xiang, W. Bao, J. Chen, T. Gao, G. Xie, Enhancing strength and ductility of pure titanium by interstitial oxygen atoms, Mater. Sci, Eng. A 14 (2022), https://doi.org/10.1016/j.msea.2022.143806

[44] D. Texier, A. Palchoudhary, J. Genée, Q. Sirvin, Y. Zhang, G. Kermouche, D. Monceau, D. Poquillon, E. Andrieu, Effect of oxygen dissolution on the mechanical behavior of thin Ti-6Al-4V specimens oxidized at high temperature: experimental and modeling approach, Corros. Sci. 235 (2024) 112177, https://doi.org/10.1016/j.corsci.2024.112177

[45] G.B. Viswanathan, E. Lee, D.M. Maher, S. Banerjee, H.L. Fraser, Direct observations and analyses of dislocation substructures in the α phase of an α/β Ti-alloy formed by nanoindentation, Acta Mater. 53 (2005) 5101–5115, https://doi.org/10.1016/j.actamat.2005.07.030

[46] T.B. Britton, H. Liang, F.P.E. Dunne, A.J. Wilkinson, The effect of crystal orientation on the indentation response of commercially pure titanium: experiments and simulations, Proc. R. Soc. A 466 (2010) 695–719, https://doi.org/10.1098/rspa.2009.0455

[47] C. Zambaldi, Y. Yang, T.R. Bieler, D. Raabe, Orientation informed nanoindentation ofα-titanium: indentation pileup in hexagonal metals deforming by prismatic slip, J. Mater. Res. 27 (2012) 356–367, https://doi.org/10.1557/jmr.2011.334

[48] C. Fizanne-Michel, M. Cornen, P. Castany, I. Péron, T. Gloriant, Determination of hardness and elastic modulus inverse pole figures of a polycrystalline commercially

pure titanium by coupling nanoindentation and EBSD techniques, Mater. Sci. Eng. A 613 (2014) 159–162, https://doi.org/10.1016/j.msea.2014.06.098
[49] J.S. Weaver, M.W. Priddy, D.L. McDowell, S.R. Kalidindi, On capturing the grain-scale elastic and plastic anisotropy of alpha-Ti with spherical nanoindentation and electron back-scattered diffraction, Acta Mater. 117 (2016) 23–34, https://doi.org/10.1016/j.actamat.2016.06.053
[50] M. Kalyan Phani, A. Kumar, W. Arnold, K. Samwer, Elastic stiffness and damping measurements in titanium alloys using atomic force acoustic microscopy, J. Alloys Compd. 676 (2016) 397–406, https://doi.org/10.1016/j.jallcom.2016.03.155
[51] Z. Liu, J. Zhang, B. He, Y. Zou, High-speed nanoindentation mapping of a near-alpha titanium alloy made by additive manufacturing, J. Mater. Res. 36 (2021) 2223–2234, https://doi.org/10.1557/s43578-021-00204-7
[52] Z. Liu, L. Lang, S.M. Mohammed, D. Chen, B. He, Y. Zou, Small-depth nanoindentation studies of an additively manufactured titanium alloy: anisotropic nanomechanical properties and correlation with microscopic mechanical behaviour, Materialia 30 (2023) 101802, https://doi.org/10.1016/j.mtla.2023.101802
[53] D. Texier, T. Richeton, H. Proudhon, A. Dziri, Q. Sirvin, M. Legros, Increase in elastic and hardness anisotropy of titanium with oxygen uptake due to high temperature oxidation: a multimodal framework using high speed nanoindentation mapping, Mater. Charact. 216 (2024) 114244, https://doi.org/10.1016/j.matchar.2024.114244
[54] J.J. Vlassak, W.D. Nix, Indentation modulus of elastically anisotropic half spaces, Philos. Mag. A 67 (1993) 1045–1056, https://doi.org/10.1080/01418619308224756
[55] J.J. Vlassak, W.D. Nix, Measuring the elastic properties of anisotropic materials by means of indentation experiments, J. Mech. Phys. Solids 42 (1994) 1223–1245, https://doi.org/10.1016/0022-5096(94)90033-7
[56] D. Texier, D. Monceau, J.-C. Salabura, R. Mainguy, E. Andrieu, Micromechanical testing of ultrathin layered material specimens at elevated temperature, Mater. High Temp. 33 (2016) 325–337, https://doi.org/10.1080/09603409.2016.1182250
[57] D. Nečas, P. Klapetek, Gwyddion: an open-source software for SPM data analysis, Cent. Eur. J. Phys. 10 (2012) 181–188, https://doi.org/10.2478/s11534-011-0096-2
[58] R. Hielscher, H. Schaeben, A novel pole figure inversion method: specification of the mtex algorithm, J. Appl. Cryst. 41 (2008) 1024–1037, https://doi.org/10.1107/S0021889808030112
[59] A. Marano, C. Ribart, H. Proudhon, Towards a data platform for multimodal 4d mechanics of material microstructures, Mater. Des. 246 (2024) 113306, https://doi.org/10.1016/j.matdes.2024.113306
[60] C. Dupressoire, A. Rouaix-Vande Put, P. Emile, C. Archambeau-Mirguet, R. Peraldi, D. Monceau, Effect of nitrogen on the kinetics of oxide scale growth and of oxygen dissolution in the ti6242s titanium-based alloy, Oxid. Met. 87 (2017) 343–353, https://doi.org/10.1007/s11085-017-9729-1
[61] K. Gautier, A. Casadebaigt, E. Fourcade, E. Epifano, T. Gaur, A. Vande Put, D. Monceau, Development and application of high-purity Ti-O reference alloys for oxygen quantification using HR-microLIBS, Materialia 44 (2025) 102545, https://doi.org/10.1016/j.mtla.2025.102545
[62] A. Paul, T. Laurila, V. Vuorinen, S.V. Divinski, Fick's Laws of Diffusion, Springer International Publishing, 2014, pp. 115–139. https://doi.org/10.1007/978-3-319-07461-0_3
[63] M. Göbel, V.A.C. Haanappel, M.F. Stroosnijder, On the determination of diffusion coefficients of oxygen in one-phase Ti (α-Ti) and two-phase Ti–4Nb (α- and β-ti) by micro-hardness measurements, Oxid. Met. 55 (2001) 137–151, https://doi.org/10.1023/A:1010333410938
[64] R. Quey, P. Dawson, F. Barbe, Large-scale 3d random polycrystals for the finite element method: generation, meshing and remeshing, Comput. Methods Appl. Mech. Eng. 200 (2011) 1729–1745, https://doi.org/10.1016/j.cma.2011.01.002
[65] R. Quey, M. Kasemer, The neper/fepx project: free /open-source polycrystal generation, deformation simulation, and post-processing, IOP Conf. Ser.: Mater. Sci. Eng. 1249 (2022) 012021, https://doi.org/10.1088/1757-899X/1249/1/012021
[66] O. Anderson, C.R. Ottermann, R. Kuschnereit, P. Hess, K. Bange, Density and Young's modulus of thin TiO_2 films, Fresenius' J. Anal. Chem. 358 (1997) 315–318, https://doi.org/10.1007/s002160050416
[67] T. Chen, S. Koyama, S. Nishida, L. Yu, Mechanical properties and frictional wear characteristic of pure titanium treated by atmospheric oxidation, Materials 14 (2021), https://doi.org/10.3390/ma14123196
[68] A. Maytorena-Sanchez, J. Hernandez-Torres, F. Lopez-Huerta, M. Hernandez-Campos, L. Zamora-Peredo, M. Pacio-Castillo, L. Serrano-De la Rosa, L. Garcia-Gonzalez, Analysis of the hardness and tribological properties of grade 2 titanium using the thermal oxidation process at different temperatures, Mater. Lett. 282 (2021) 128679, https://doi.org/10.1016/j.matlet.2020.128679
[69] Z-set Software, Z-set non-linear material and structure analysis suite, 2025, http://zset-software.com
[70] J.-D. Garaud, J. Rannou, C. Bovet, S. Feld-Payet, V. Chiaruttini, B. Marchand, L. Lacourt, V.A. Yastrebov, N. Osipov, S. Quilici, Z-set -suite logicielle pour la simulation des matériaux et structures, CSMA2019: 14ème Colloque National en Calcl des Structures (2019), https://hal.science/hal-02115875v1
[71] M. Tournay, J.-S. Lecomte, C. Schuman, Y. Zhang, É. Fleury, Achieving basal texture in pure titanium: process implementation and mechanical property evaluation, Mater. Charact. 223 (2025) 114898, https://doi.org/10.1016/j.matchar.2025.114898
[72] P. Kofstad, P. Anderson, O. Krudtaa, Oxidation of titanium in the temperature range 800–1200°C, J. Less-Common Met. 3 (1961) 89–97, https://doi.org/10.1016/0022-5088(61)90001-7
[73] D. David, G. Béranger, E.A. García, A study of the diffusion of oxygen in α-titanium oxidized in the temperature range 460°-700°C, J. Electrochem. Soc. 130 (1983) 1423, https://doi.org/10.1002/chin.198339013
[74] X. Chen, L. Huang, Y. Jiao, S. Wang, Q. An, Y. Bao, L. Geng, Mechanisms of oxidation anisotropy between α-ti (0001) and $(01\bar{1}0)$ crystallographic planes in titanium matrix composites, Mater. Lett. 286 (2021) 129230, https://doi.org/10.1016/j.matlet.2020.129230